

Supporting Information

for the article

Addressing Reversibility of R-NHC Coupling on Palladium: Is Nano-to-Molecular Transition Possible for the Pd/NHC System?

Ekaterina A. Denisova, Dmitry B. Eremin, Evgeniy G. Gordeev, Andrey M. Tsedilin and Valentine P. Ananikov

Zelinsky Institute of Organic Chemistry, Russian Academy of Sciences, Leninsky Prospect 47, Moscow 119991, Russia

S1. R,R'-NHC COUPLING REACTION CONDITIONS	S2
S2. NMR SPECTRA	S5
S3. MASS SPECTRA	S12
S4. TEM EXPERIMENTS	S20
S5. THEORETICAL CALCULATIONS.....	S23

S1. R,R'-NHC coupling reaction conditions

Table S1. Mass-spectrometric study of reversibility of R-NHC coupling.

Entry	[Pd] 1 eq.	Intens. [NHC-Ph] ⁺ /[NHC-Me] ⁺ ^(a)		
		No base / Et ₃ N	No base	Et ₃ N
		0 h ^(b)	24 h ^(c)	24 h
1	Pd(OAc) ₂	nd	high	trace
2	Pd(OAc) ₂ + 2 eq. PPh ₃	nd	average	nd
3	Pd(acac) ₂	nd	average	nd
4	Pd ₂ dba ₃ ·CHCl ₃	nd	nd	nd
5	PdCl ₂ (PPh ₃) ₂	nd	trace	nd
6	PdCl ₂	nd	nd	nd
7	PdI ₂	nd	trace	nd
8	No [Pd]	nd	nd	nd

^(a) ESI-MS, $I = I_{[\text{NHC-Ph}]^+}/I_{[\text{NHC-Me}]^+}$: 0.1 < I < 0.3 – small, 0.3 < I < 0.5 – average, I > 1 – high; nd – not detected with reasonable intensity;

^(b) after mixing before heating; ^(c) after 24 h of heating.

Table S2. ¹H NMR-spectroscopic study of reversibility of R-NHC coupling.

Entry	1 eq. [Pd]	Conversion, %	Yield, %
1	Pd(OAc) ₂	72	31
2	Pd(OAc) ₂ + 2 eq. PPh ₃	66	24
3	Pd(acac) ₂	36	13
4	No [Pd]	7	0

Table S3. Observation of the reversibility of R-NHC coupling under various conditions.

Entry	Variable parameter		ESI-MS ^(a)		¹ H NMR	
			Intens. ^(b) [NHC-Ph] ⁺ / [NHC-Me] ⁺	Intens. ^(c) [NHC-Ph] ⁺ / [NHC-Me] ⁺	Conversion of 1 ^(c) , %	Yield of 2 ^(c) , %
1	ArX	(<i>p</i> -OMe)C ₆ H ₄ I	nd	high	60	44
2		(<i>p</i> -NO ₂)C ₆ H ₄ I	nd	small	44	12
3		PhBr	trace	high	60	16
4		PhCl	trace	trace	37	0
5	1a to PhI ratio	1:1	nd	high	60	43
6		1:2	trace	high	72	31
7	Pd(OAc) ₂ loading	5 mol %	nd	trace	10	<1
8		10 mol %	nd	trace	12	1
9		50 mol %	nd	average	35	20
10	Azolium salt	1b	nd	average	56	56
11		1c	nd	average	34	34

^(a) ESI-MS, $I = I_{[\text{NHC-Ph}]^+}/I_{[\text{NHC-Me}]^+}$: 0.1 < I < 0.3 – small, 0.3 < I < 0.5 – average, I > 1 – high; nd – not detected with reasonable intensity;

^(b) after mixing before heating; ^(c) after 24 h of heating.

Table S4. Observation of the reversibility of R-NHC coupling in the presence of different metals.

Entry	[M] 1 eq.	ESI-MS		¹ H NMR
		Intens. ^(a)		
		[NHC-Ph] ⁺ /[NHC-Me] ⁺		
0 h ^(b)	24 h ^(c)			
1	CuOAc	nd	high	80
2	CuOAc + 2 eq. PPh ₃	nd	high	74
3	Cu(acac) ₂	nd	high	33
4	Ni(OAc) ₂ ·4H ₂ O	nd	nd	nd ^(d)
5	Ni(OAc) ₂ ·4H ₂ O + 2 eq. PPh ₃	nd	trace	nd ^(d)
6	Ni(acac) ₂	nd	average	10
7	Ni(NO ₃) ₂ ·6H ₂ O	nd	small	3
8	Co(OAc) ₂	nd	nd	-
9	Co(OAc) ₂ + 2 eq. PPh ₃	nd	nd	-
10	Co(acac) ₂	nd	nd	-
11	Co(NO ₃) ₂ ·6H ₂ O	nd	nd	-
12	Without a metal (control experiment)	nd	nd	-

^(a) ESI-MS, $I = I_{[\text{NHC-Ph}]^+} / I_{[\text{NHC-Me}]^+}$, where $0.1 < I < 0.3$ – small, $0.3 < I < 0.5$ – average, $I > 1$ – high; nd – not detected with reasonable intensity;
^(b) after mixing before heating; ^(c) after 24 h heating; ^(d) broad signals in the ¹H NMR spectrum.

S2. NMR spectra

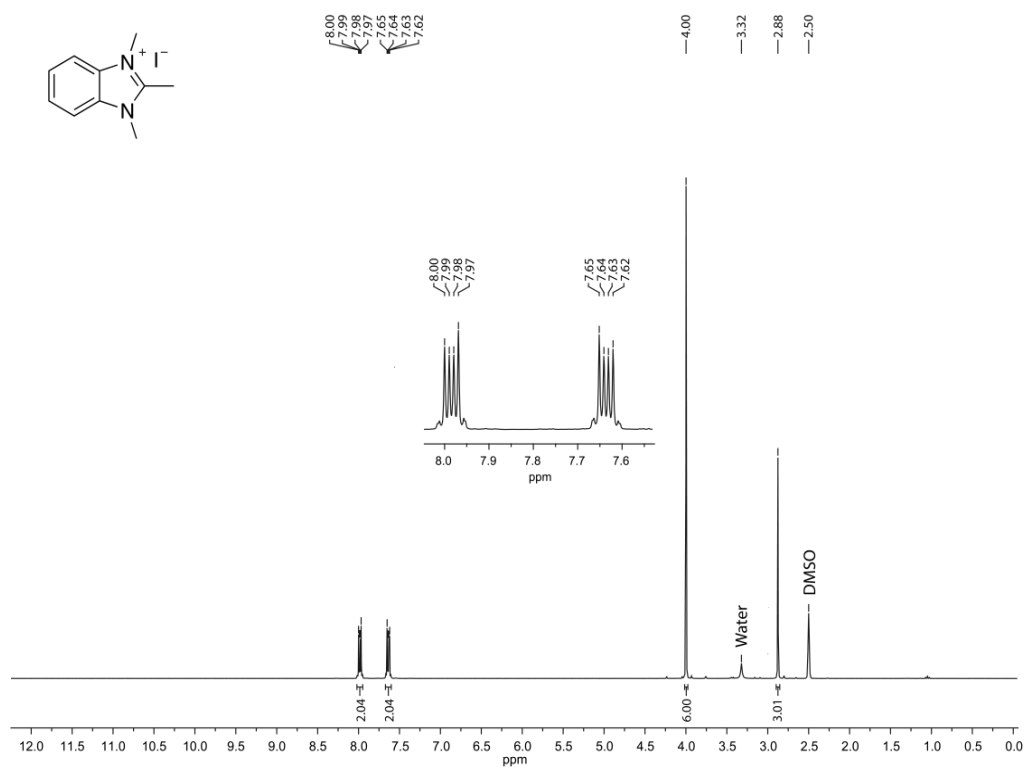


Figure S1. ^1H NMR spectrum of **1a** (DMSO- d_6 , 300 MHz).

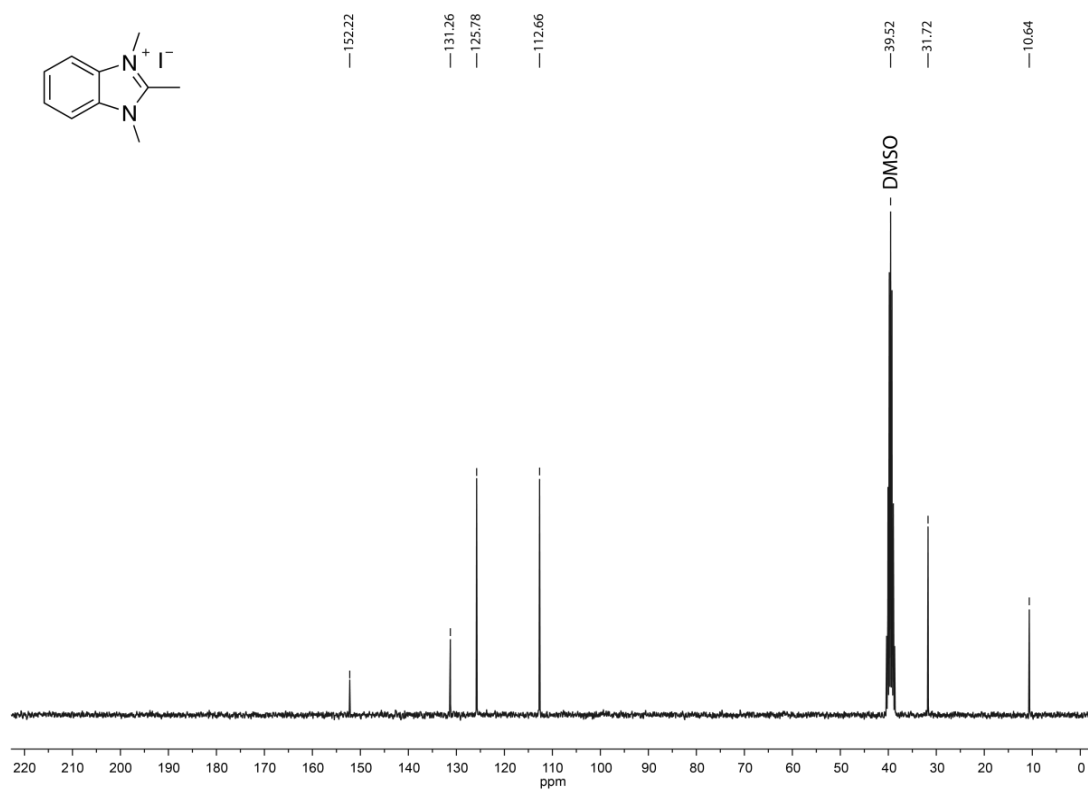


Figure S2. $^{13}\text{C}\{^1\text{H}\}$ NMR spectrum of **1a** (DMSO- d_6 , 75 MHz).

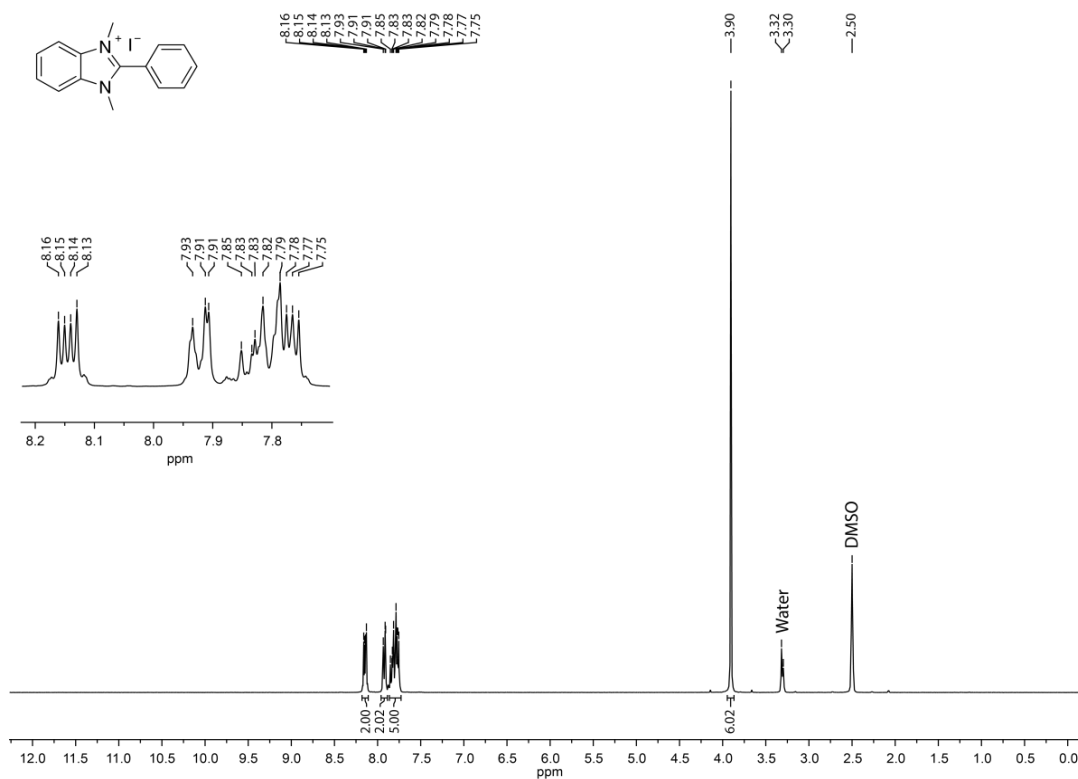


Figure S3. ^1H NMR spectrum of 2a (DMSO- d_6 , 300 MHz).

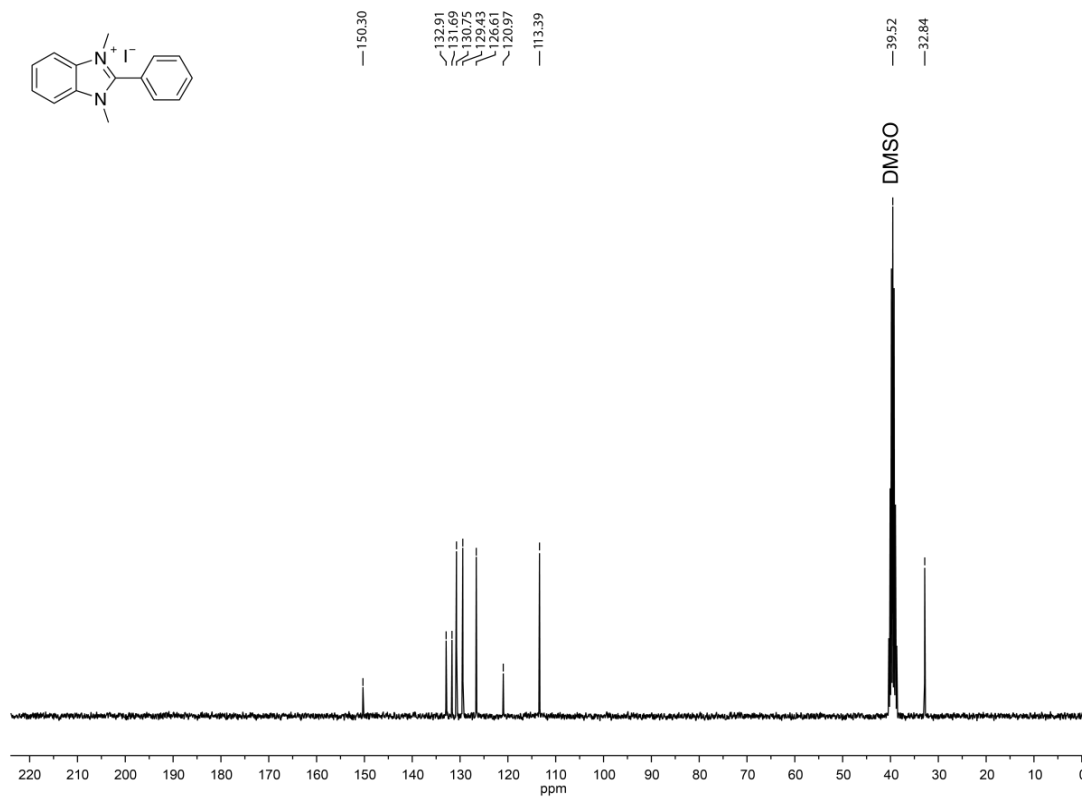


Figure S4. $^{13}\text{C}\{^1\text{H}\}$ NMR spectrum of 2a (DMSO- d_6 , 75 MHz).

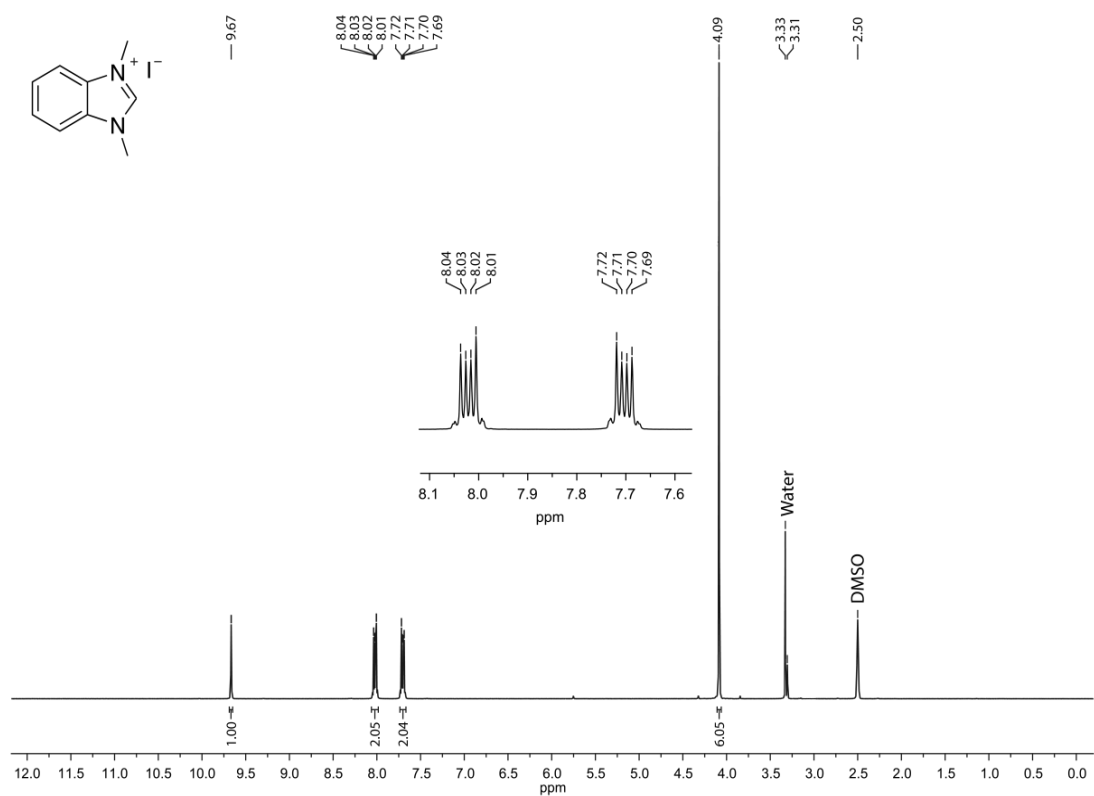


Figure S5. ¹H NMR spectrum of 1,3-dimethyl-1*H*-benzimidazol-3-ium iodide (DMSO-*d*₆, 300 MHz).

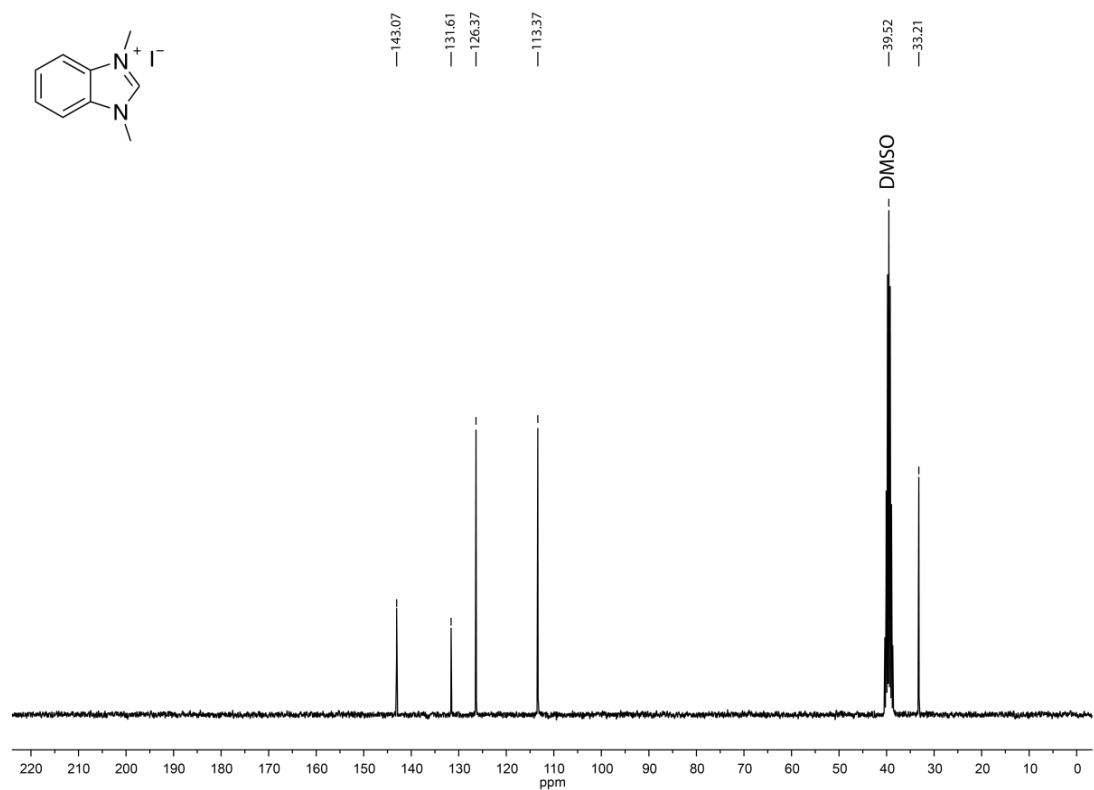


Figure S6. ¹³C{¹H} NMR spectrum of 1,3-dimethyl-1*H*-benzimidazol-3-ium iodide (DMSO-*d*₆, 75 MHz).

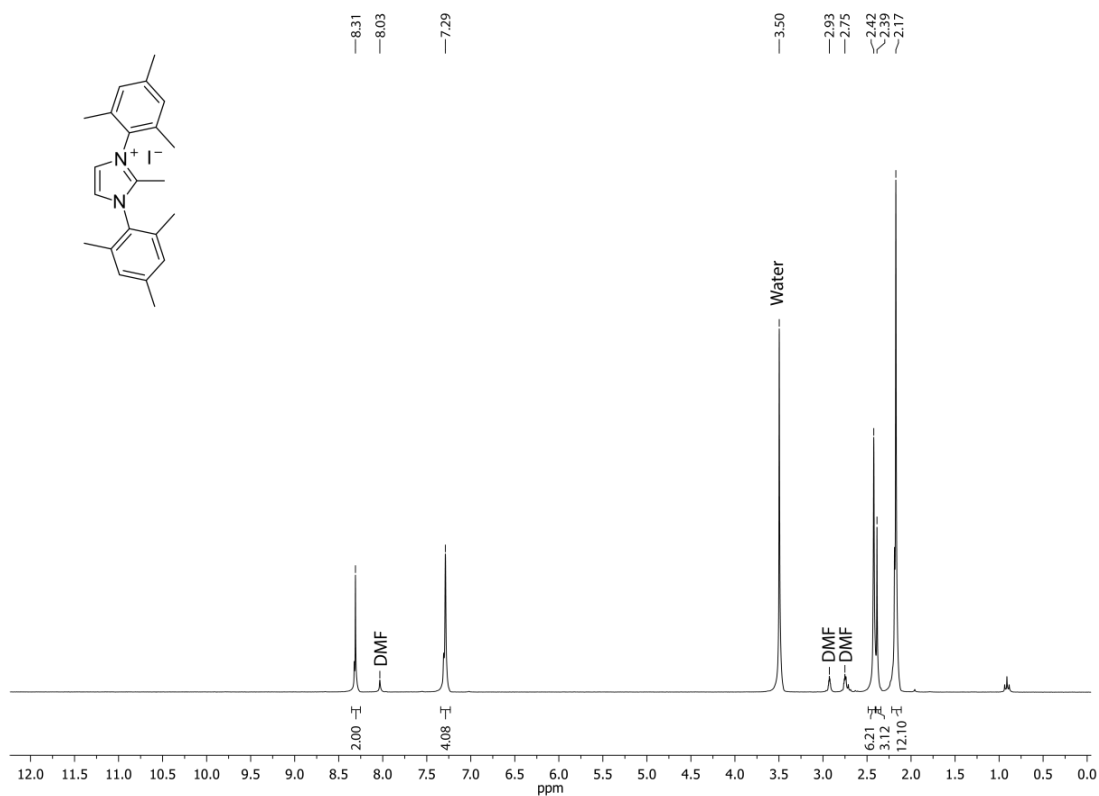


Figure S7. ^1H NMR spectrum of **1b** ($\text{DMF-}d_7$, 300 MHz).

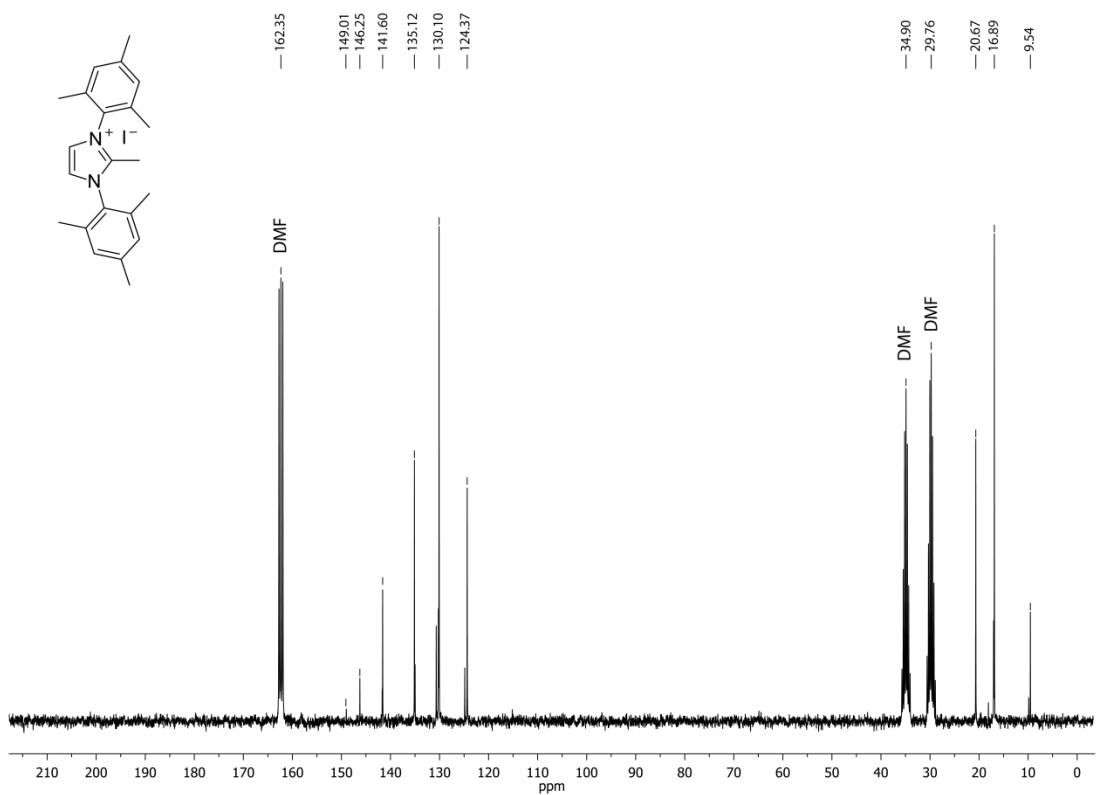


Figure S8. $^{13}\text{C}\{^1\text{H}\}$ NMR spectrum of **1b** ($\text{DMF-}d_7$, 75 MHz).

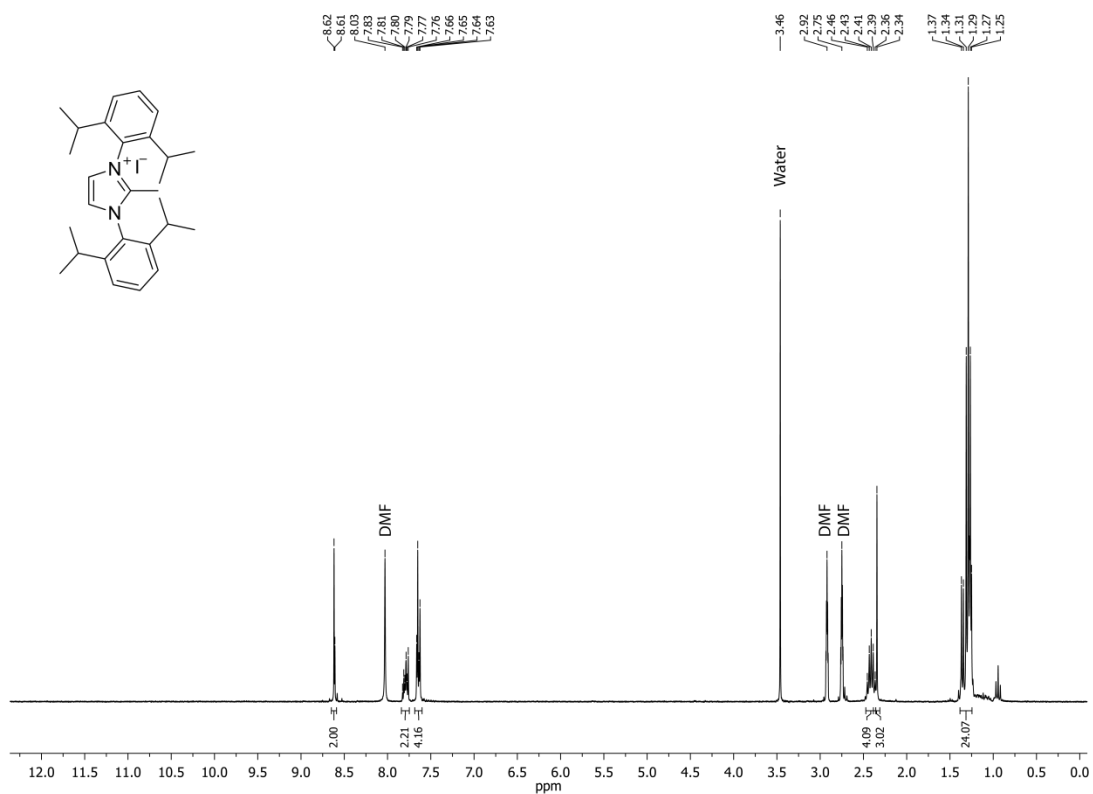


Figure S9. ¹H NMR spectrum of **1c** (DMF-*d*₇, 300 MHz); it is likely that compound **1c** has a minor spatial isomer present as evident from the spectra, the compound was confirmed by ESI-MS and elemental analysis.

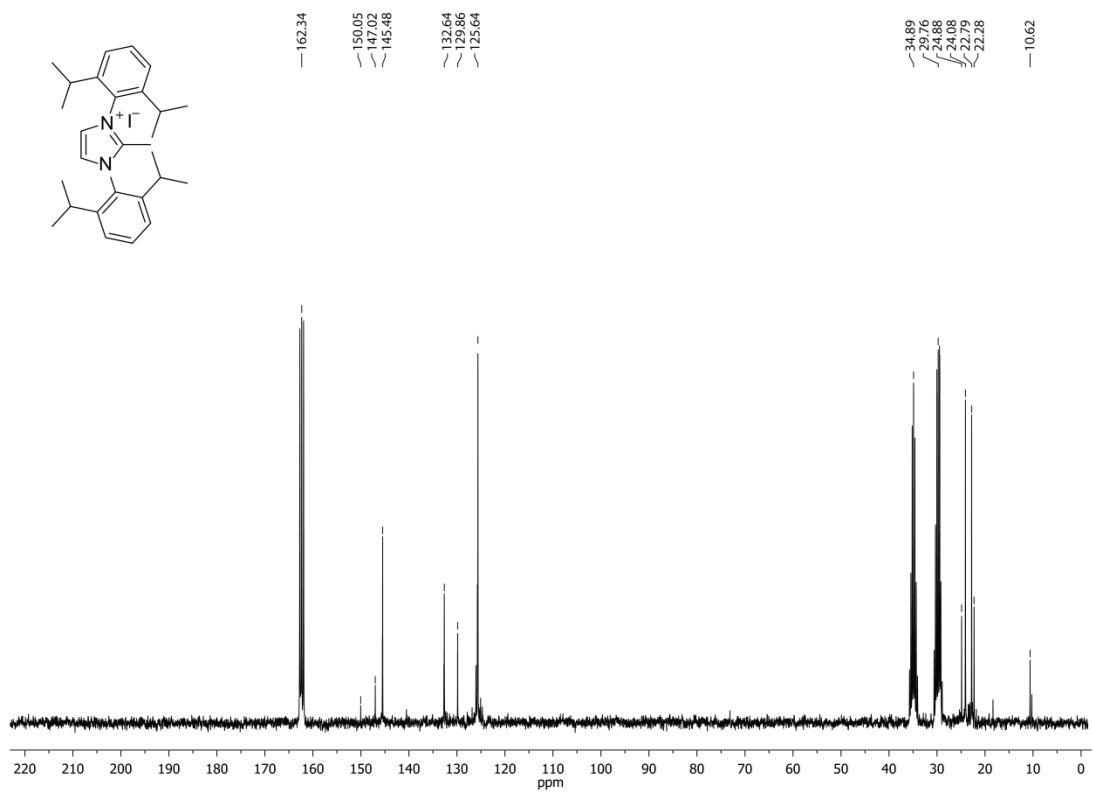


Figure S10. ¹³C{¹H} NMR spectrum of **1c** (DMF-*d*₇, 75 MHz).

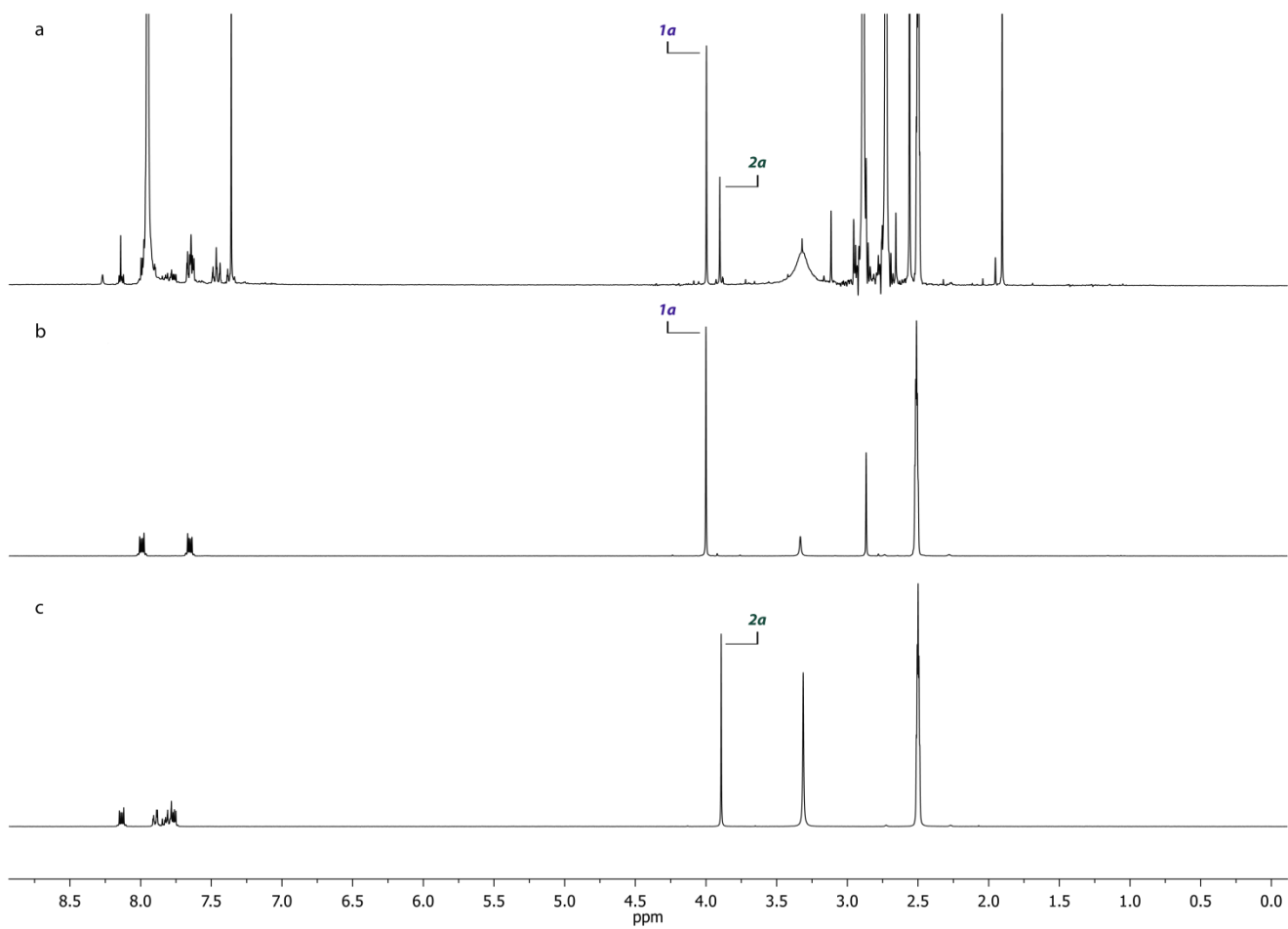


Figure S11. Comparison of signals in ¹H NMR spectra: ^(a) Reaction mixture after heating in DMSO-*d*₆: 0.1 mmol **1a**, 0.2 mmol PhI, 0.1 mmol Pd(OAc)₂, DMF, 140 °C; ^(b) Compound **1a** in DMSO-*d*₆; ^(c) Compound **2a** in DMSO-*d*₆.

S3. Mass spectra

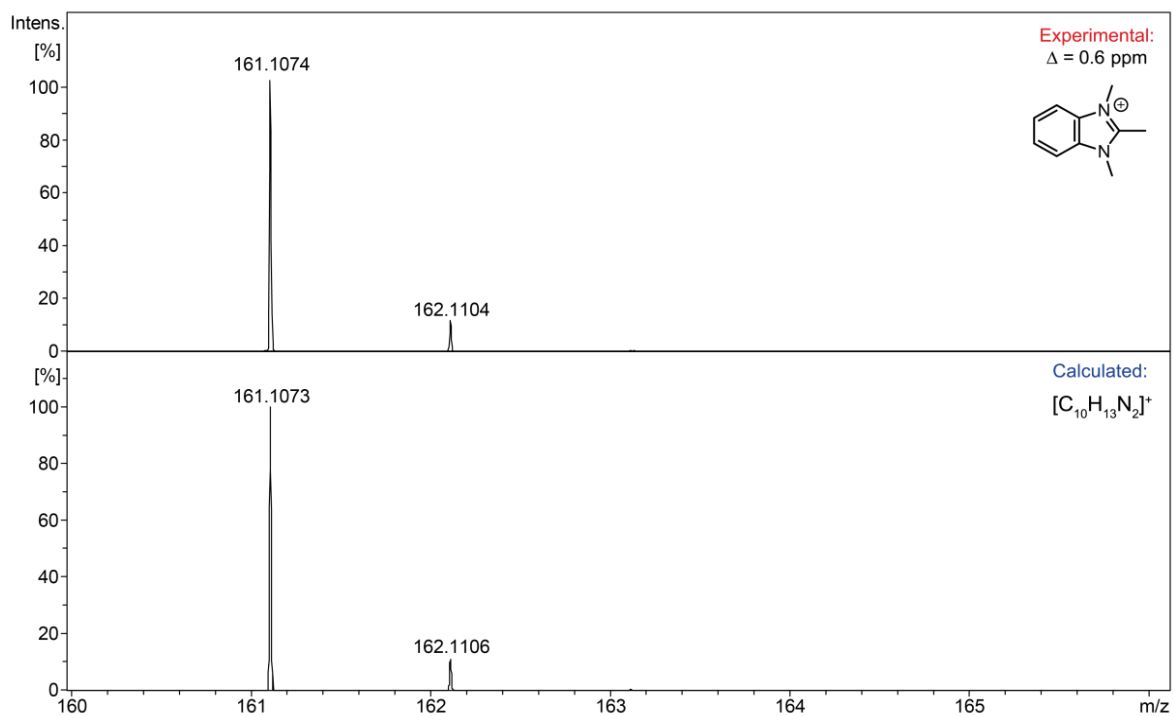


Figure S12. ESI-(+)MS spectrum of **1a** in CH_3CN solution expanded to the $[M - I]^+$ region.

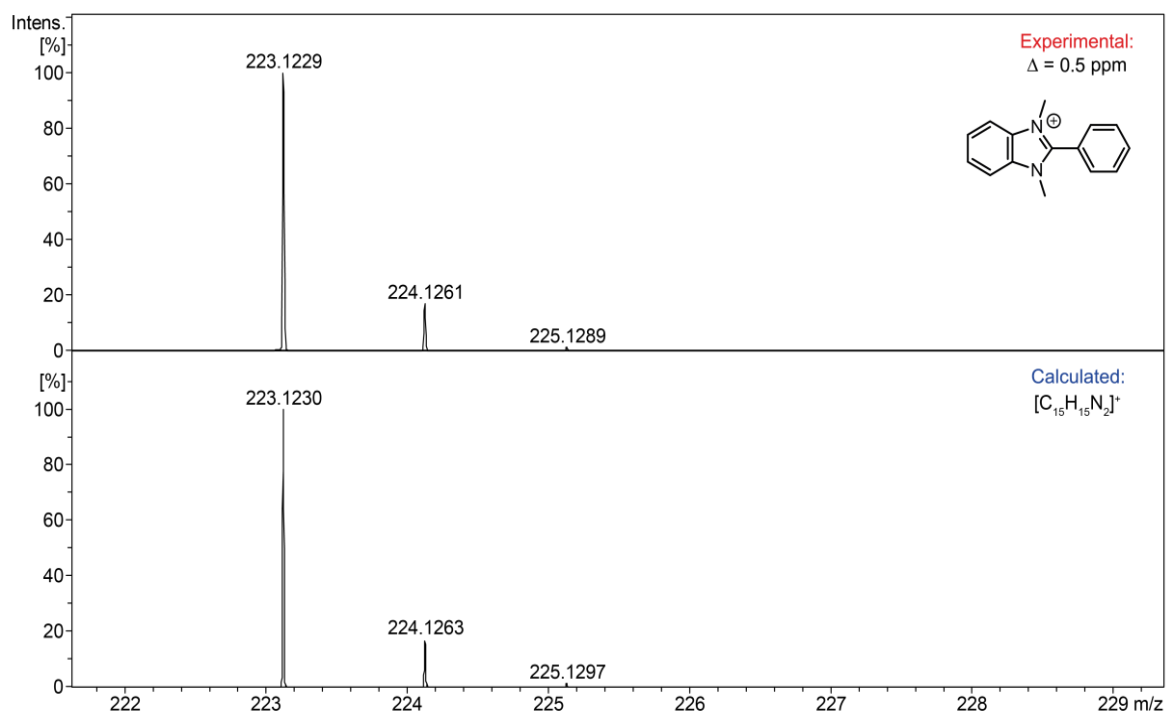


Figure S13. ESI-(+)MS spectrum of **2a** in CH_3CN solution expanded to the $[M - I]^+$ region.

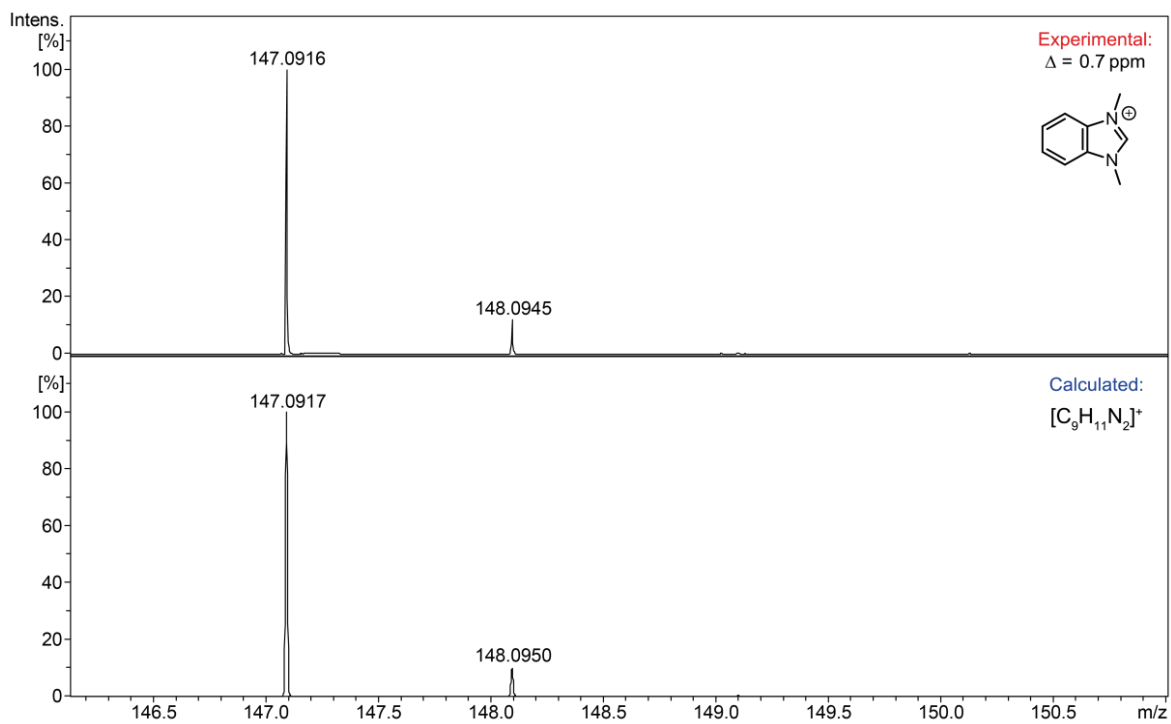


Figure S14. ESI-(+)MS spectrum of 1,3-dimethyl-1*H*-benzo[d]imidazol-3-ium iodide in CH_3CN solution expanded to the $[M - I]^+$ region.

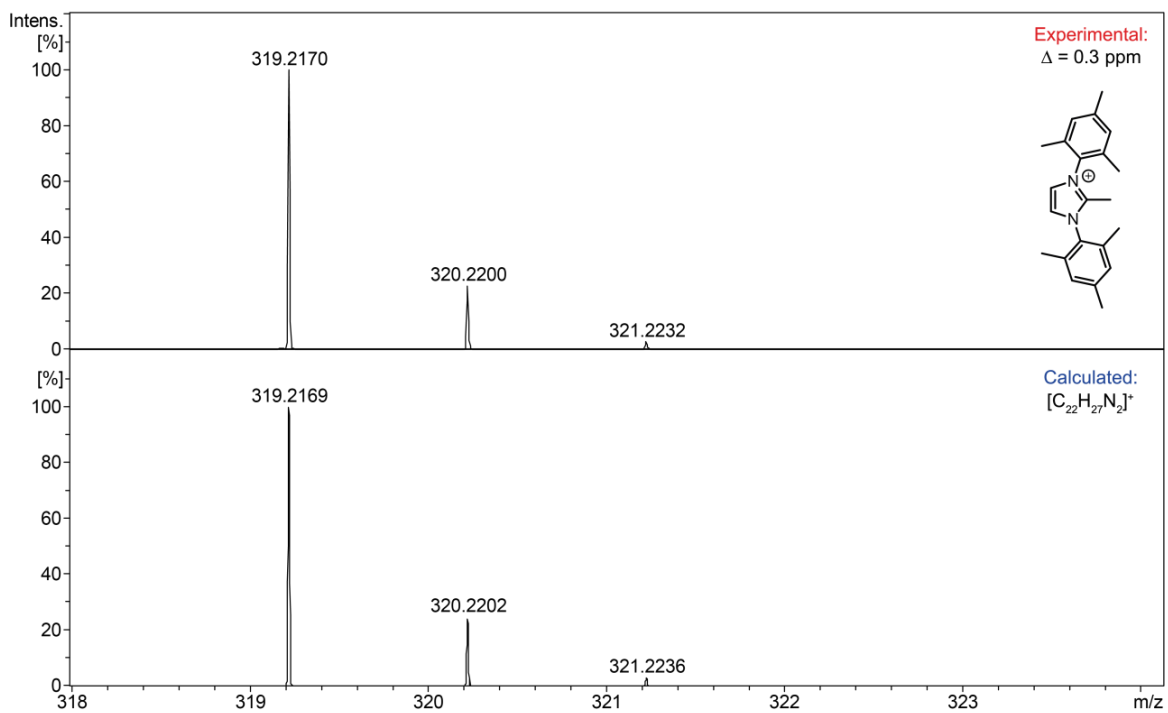


Figure S15. ESI-(+)MS spectrum of **1b** in CH_3CN solution expanded to the $[M - I]^+$ region.

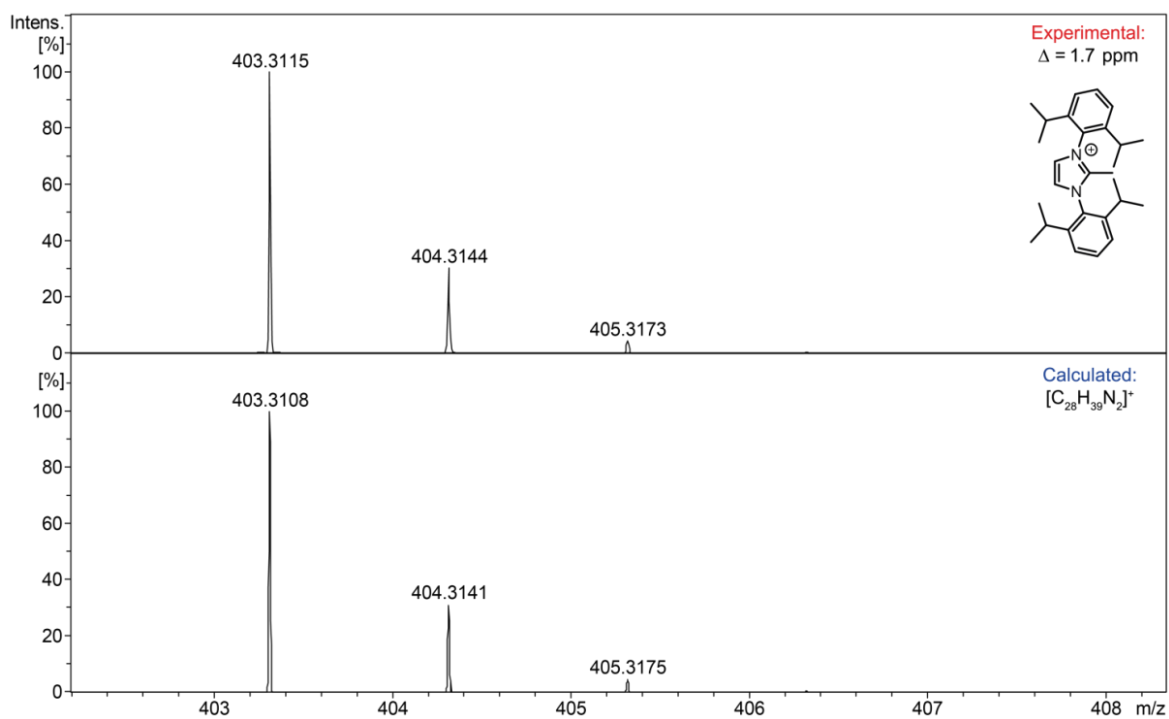


Figure S16. ESI-(+)MS spectrum of **1c** in CH_3CN solution expanded to the $[M - I]^+$ region.

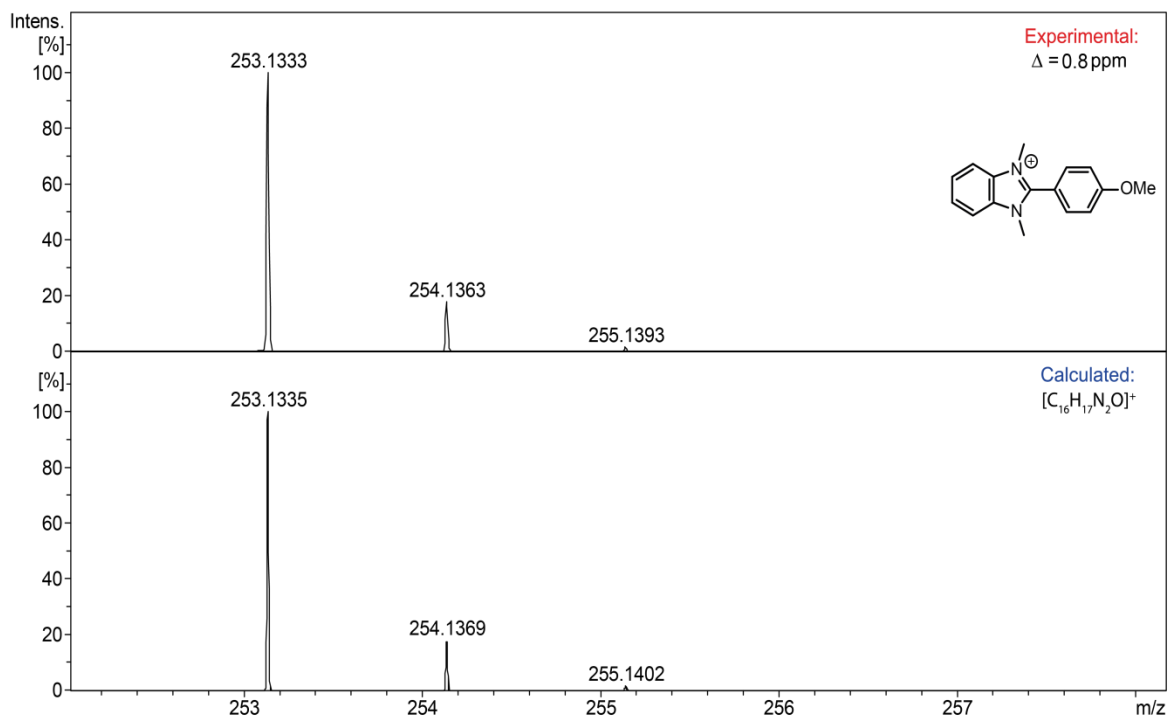


Figure S17. ESI-(+)MS spectrum of 2-(4-methoxyphenyl)-1,3-dimethyl-1*H*-benzimidazol-3-ium iodide in CH_3CN solution expanded to the $[M - I]^+$ region.

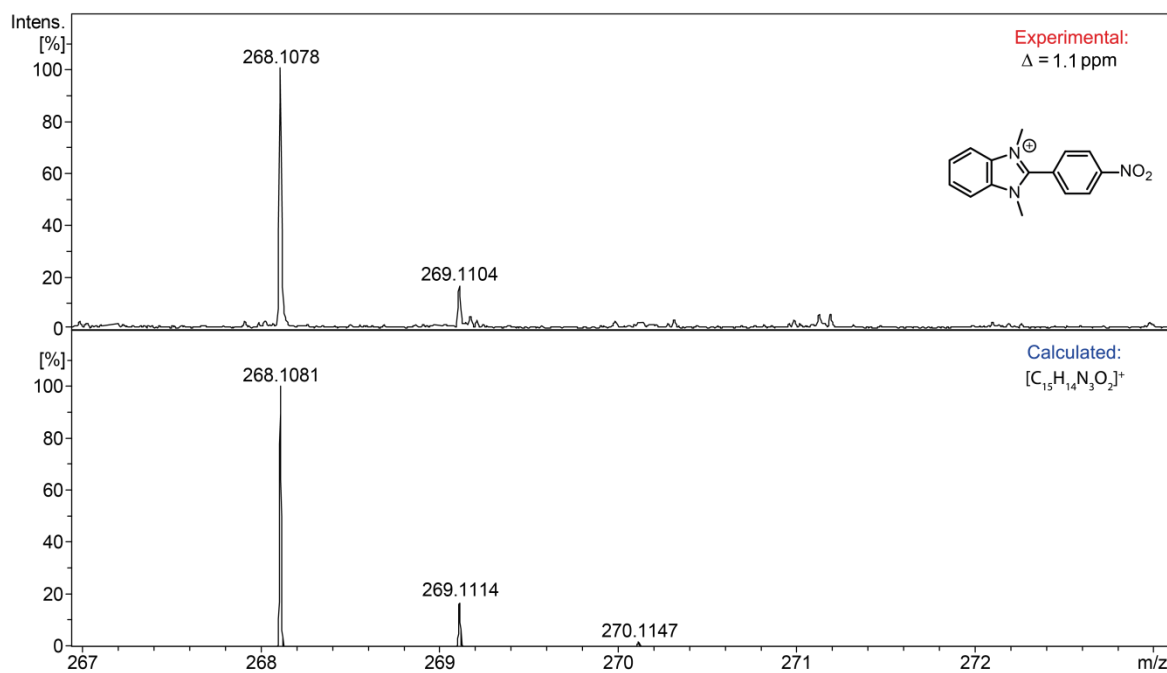


Figure S18. ESI-(+)MS spectrum of 1,3-dimethyl-2-(4-nitrophenyl)-1*H*-benzimidazol-3-ium iodide in CH_3CN solution expanded to the $[\text{M} - \text{I}]^+$ region.

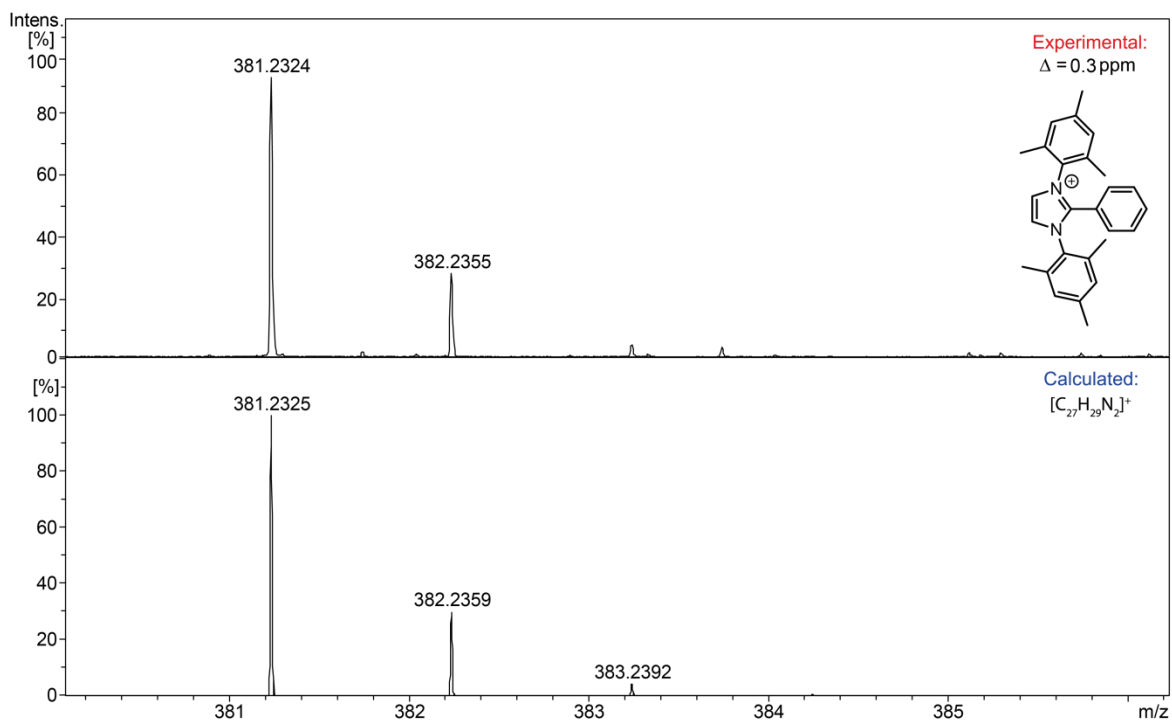


Figure S19. ESI-(+)MS spectrum of **2b** in CH_3CN solution expanded to the $[\text{M} - \text{I}]^+$ region.

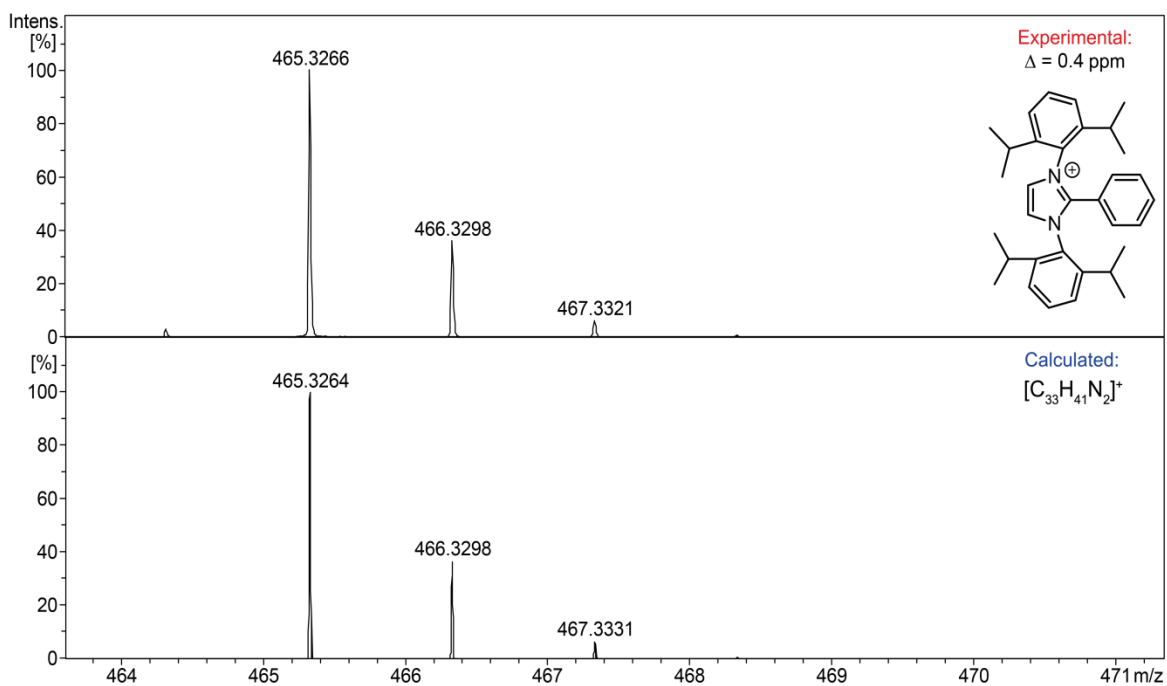


Figure S20. ESI-(+)MS spectrum of **2c** in CH_3CN solution expanded to the $[M - I]^+$ region.

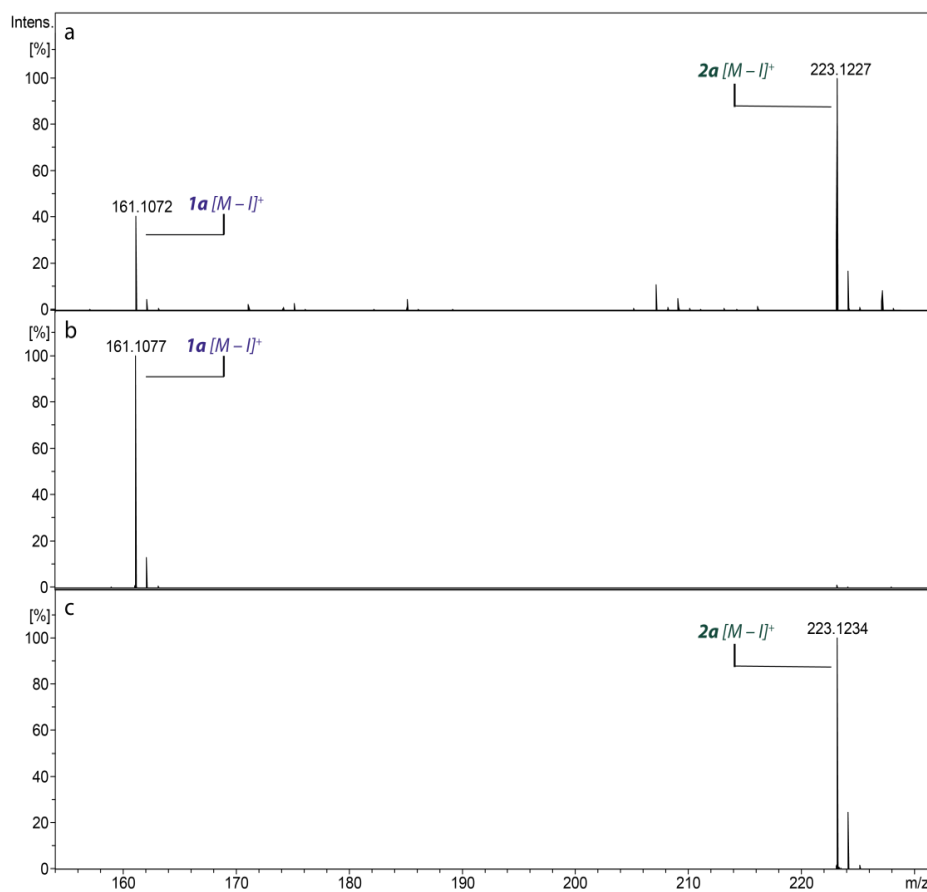


Figure S21. Comparison of signals in ESI-(+)MS spectra: (a) Reaction mixture after 24 h in CH_3CN solution expanded to the $[M - I]^+$ region: 0.1 mmol **1a**, 0.2 mmol PhI, 0.1 mmol $Pd(OAc)_2$, DMF, $140^\circ C$; (b) Compound **1a** in CH_3CN solution expanded to the $[M - I]^+$ region; (c) Compound **2a** in CH_3CN solution expanded to the $[M - I]^+$ region.

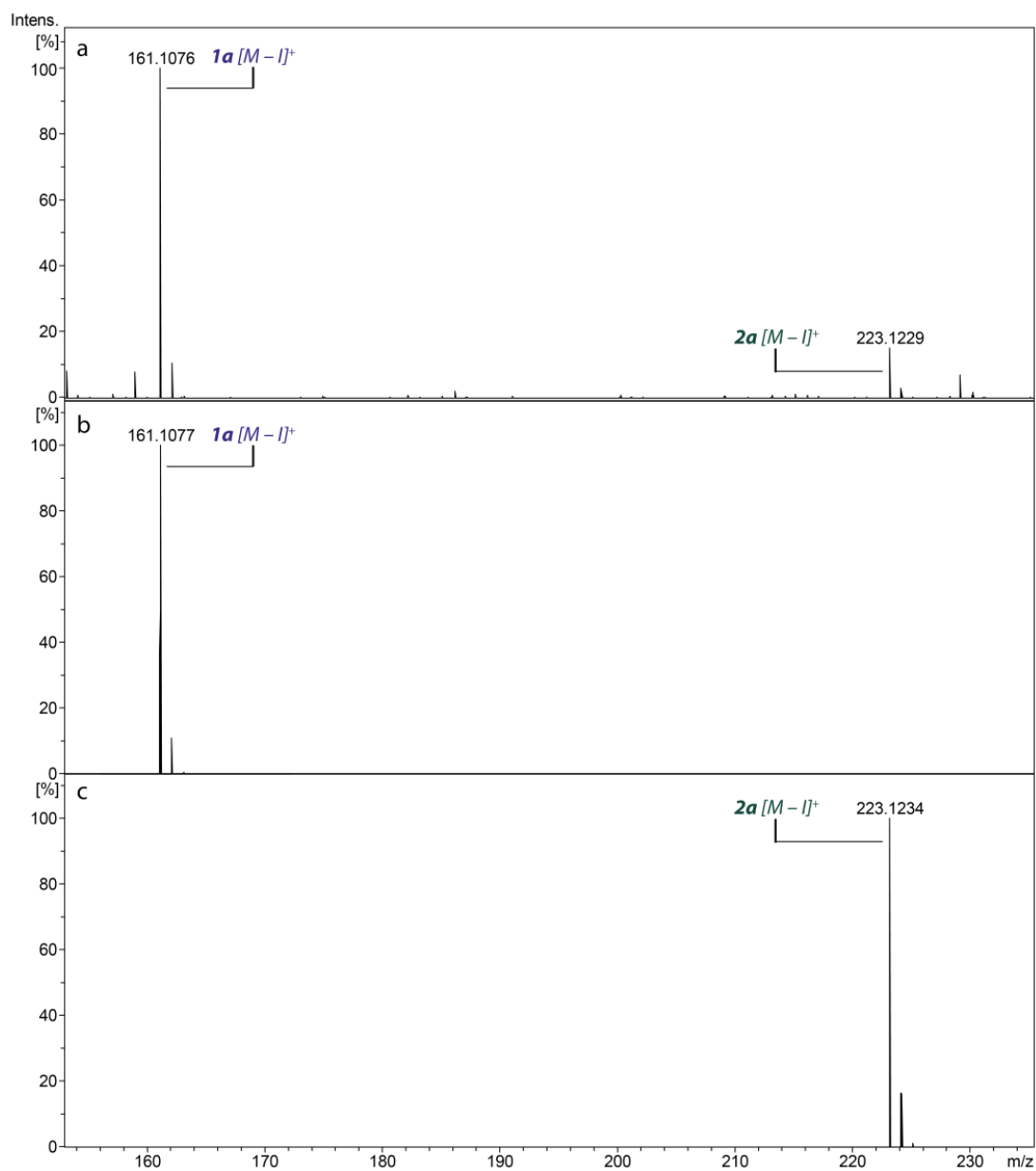


Figure S22. Comparison of signals in ESI-(+)MS spectra: (a) Reaction mixture after 24 h in CH_3CN solution expanded to the $[M-I]^+$ region: 0.1 mmol **1a**, 0.2 mmol PhI, Pd NPs preparation from 0.1 mmol $\text{Pd}(\text{OAc})_2$, DMF, 140 °C; (b) Compound **1a** in CH_3CN solution expanded to the $[M-I]^+$ region; (c) Compound **2a** in CH_3CN solution expanded to the $[M-I]^+$ region.

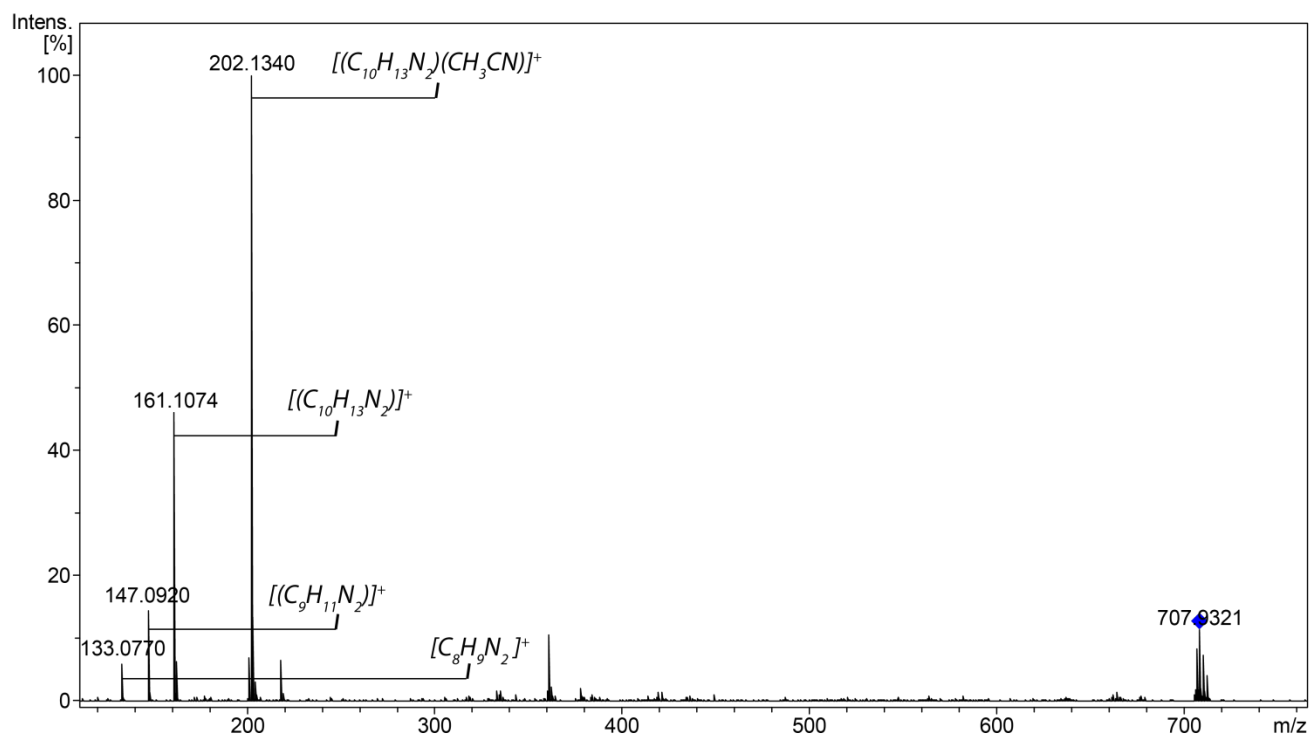


Figure S23. Collision-induced dissociation ESI-(+) MS² spectrum of $[(C_9H_{10}N_2)(C_{10}H_{13}N_2)I_2Pd(CH_3CN)]^+$ at collision energy of 20 eV.

S4. TEM experiments

1. Pd NPs formation under in DMF at various temperatures

The possibility of palladium nanoparticles formation at lower temperature in DMF was studied according to the following procedure: Pd(OAc)₂ (2 mg, 0.009 mmol) in 4 ml of DMF was heated for 1 hour at the corresponding temperature. Then, the samples for TEM analysis were prepared. According to TEM study, Pd NPs are not formed in noticeable amounts at room temperature (Figure S24, A) and only traces may be expected at 50 °C (Figure S24, B). Pd NPs were already formed at 75 °C (Figure S24, C) and at 100 °C (Figure S24, D), where the particles are clearly visible as both agglomerates and individual nanoparticles.

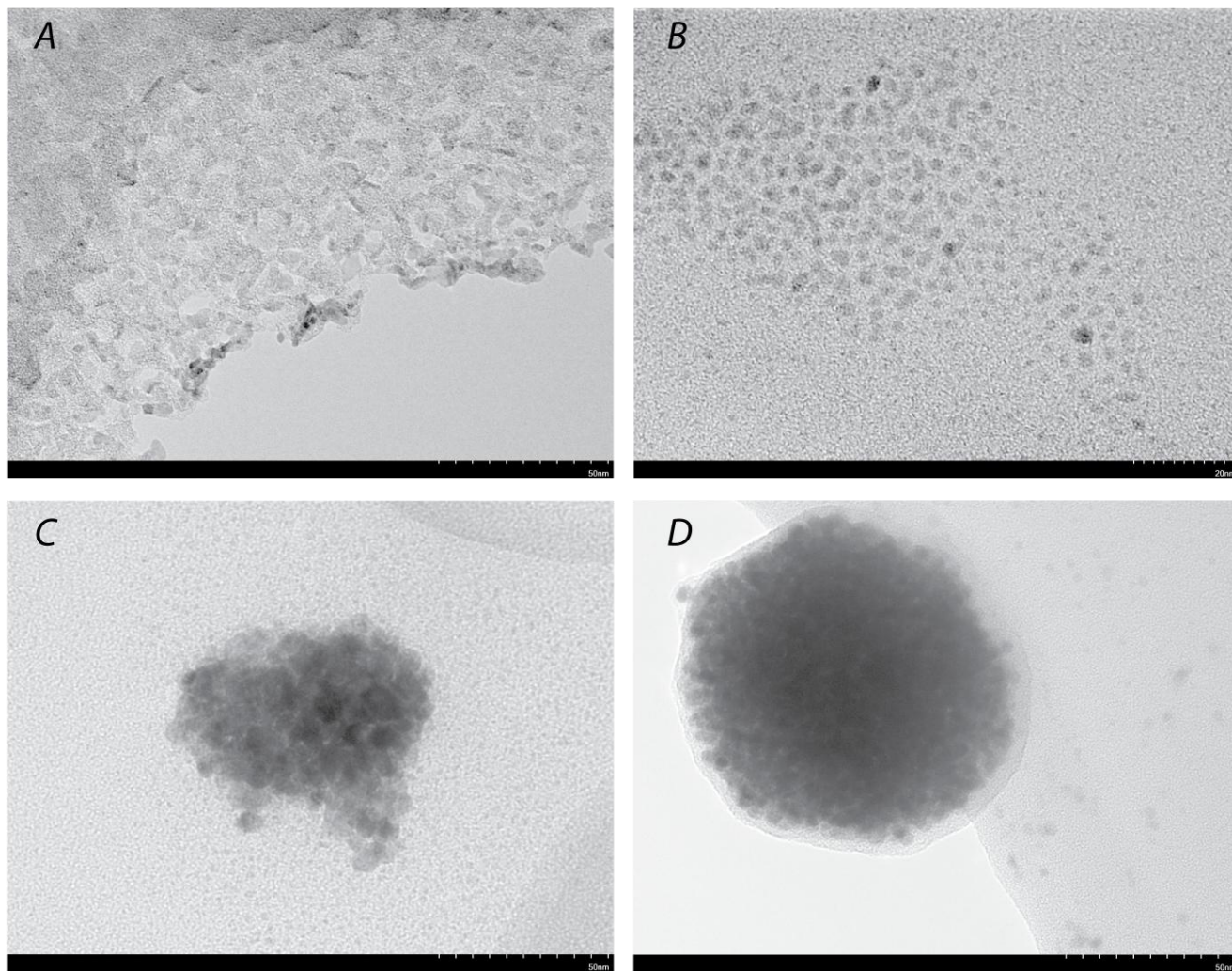


Figure S24. TEM images of Pd NPs formed from Pd(OAc)₂ in DMF at different temperatures: A – at 25 °C, scale bar 50 nm; B – at 50 °C, scale bar 20 nm; C – at 75 °C, scale bar 50 nm; D – at 100 °C, scale bar 50 nm.

2. Preparation of Pd NPs for R,R'-coupling reaction

$\text{Pd}(\text{OAc})_2$ (22.5 mg, 0.1 mmol) in 7 ml of DMF was heated for 5 min at 140 °C. Then the resulting cloudy colloidal solution was centrifuged at 6000 RPM. After that, the solution above the precipitated nanoparticles was separated and again held for 5 min at 140 °C, followed by centrifugation to separate new portion of nanoparticles. The operation was repeated 5 times until the solution stopped becoming cloudy during the heating process. The combined fractions of nanoparticles were washed with DMF and used in the reaction without further drying (to minimize agglomeration during drying process). Electron microscopy characterization is shown on Figure S25.

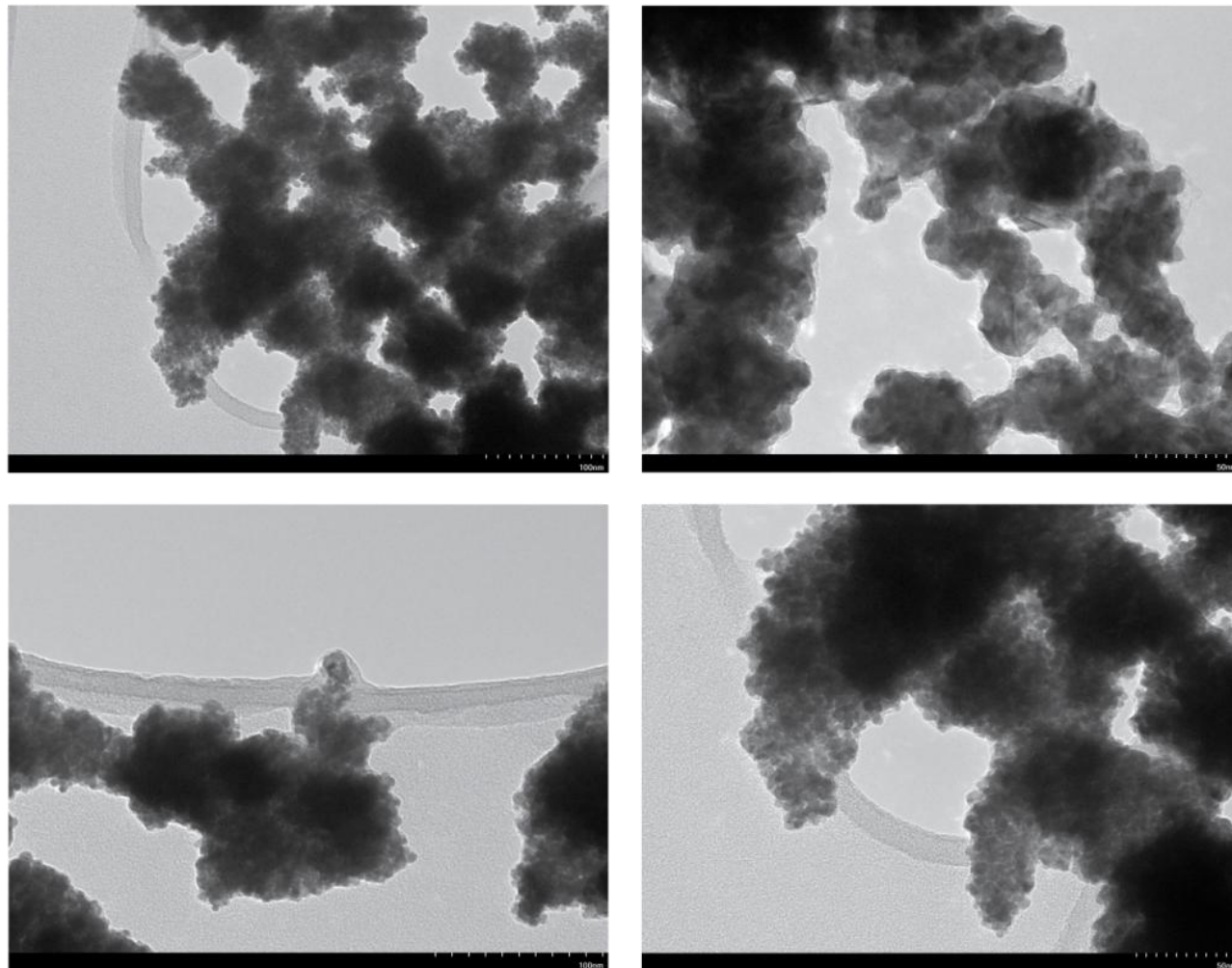


Figure S25. TEM images for Pd NPs formed from $\text{Pd}(\text{OAc})_2$ in DMF at 140 °C, scale bar for left column 100 nm, scale bar for right column is 50 nm.

S5. Theoretical calculations

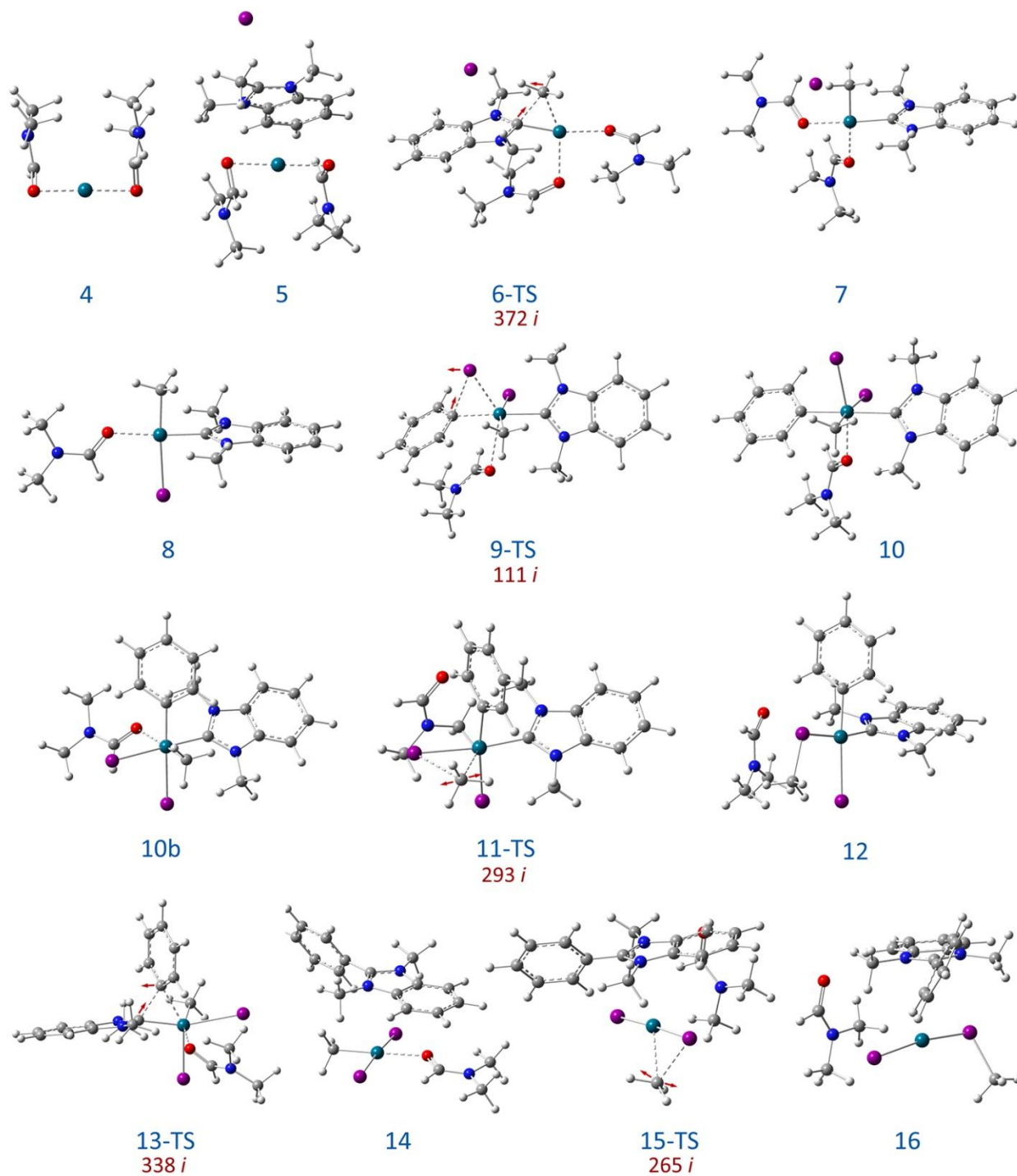


Figure S27. Optimized molecular structures of 4-16. The imaginary frequencies and atomic displacements corresponding to imaginary vibration are represented for each transition state; PBE1PBE/6-311G(d)&def2TZVP D3BJ.

3. Ph-NHC coupling involving Pd(II) dimer

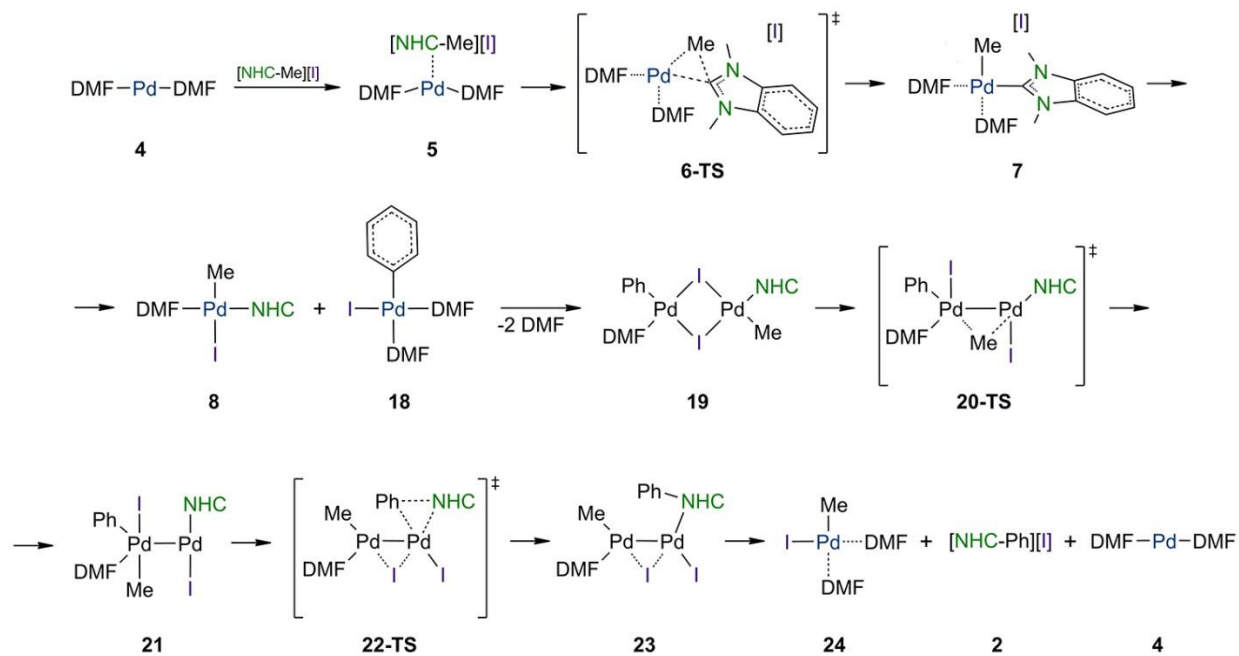


Figure S28. Reaction Ph-NHC coupling involving the Pd(II) dimer. See Figure S30 for conformational analysis of complexes **18** and **24**.

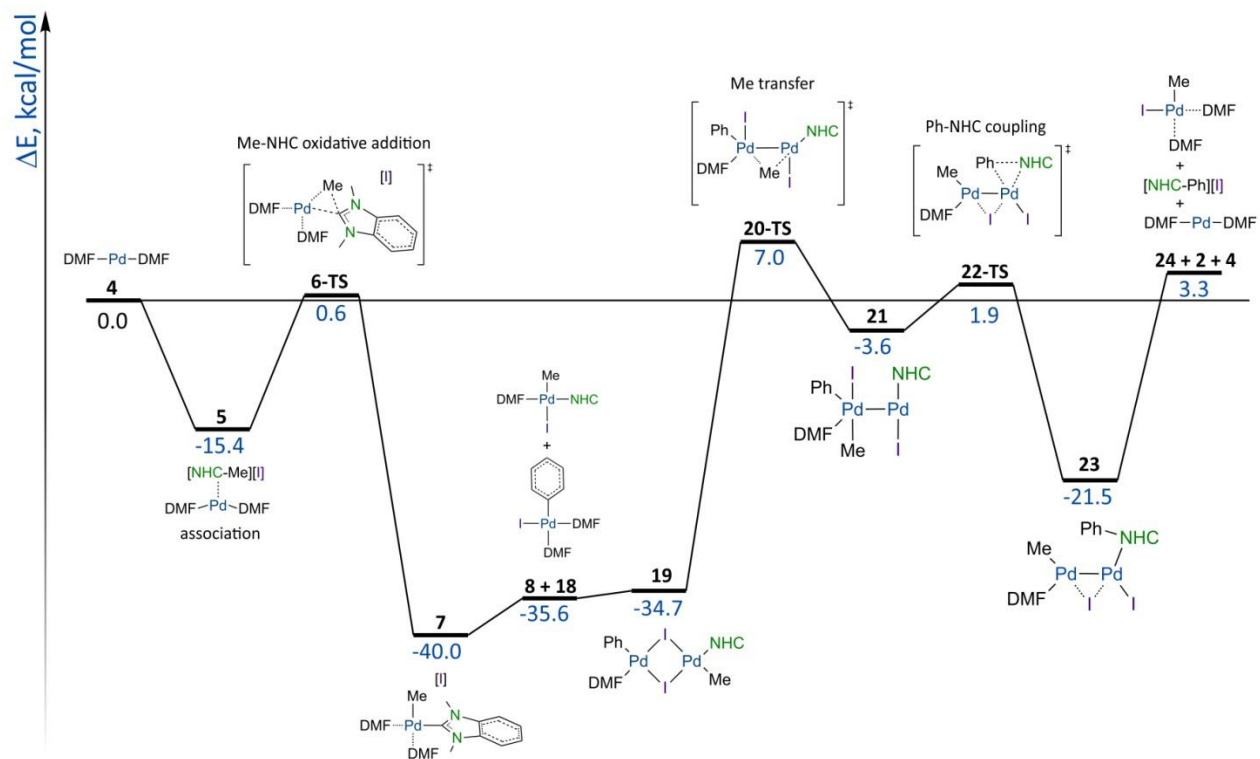


Figure S29. Profile of change in total energy during Ph-NHC coupling reaction, involving Pd(II) dimer; PBE1PBE/6-311G(d)&def2TZVP D3BJ.

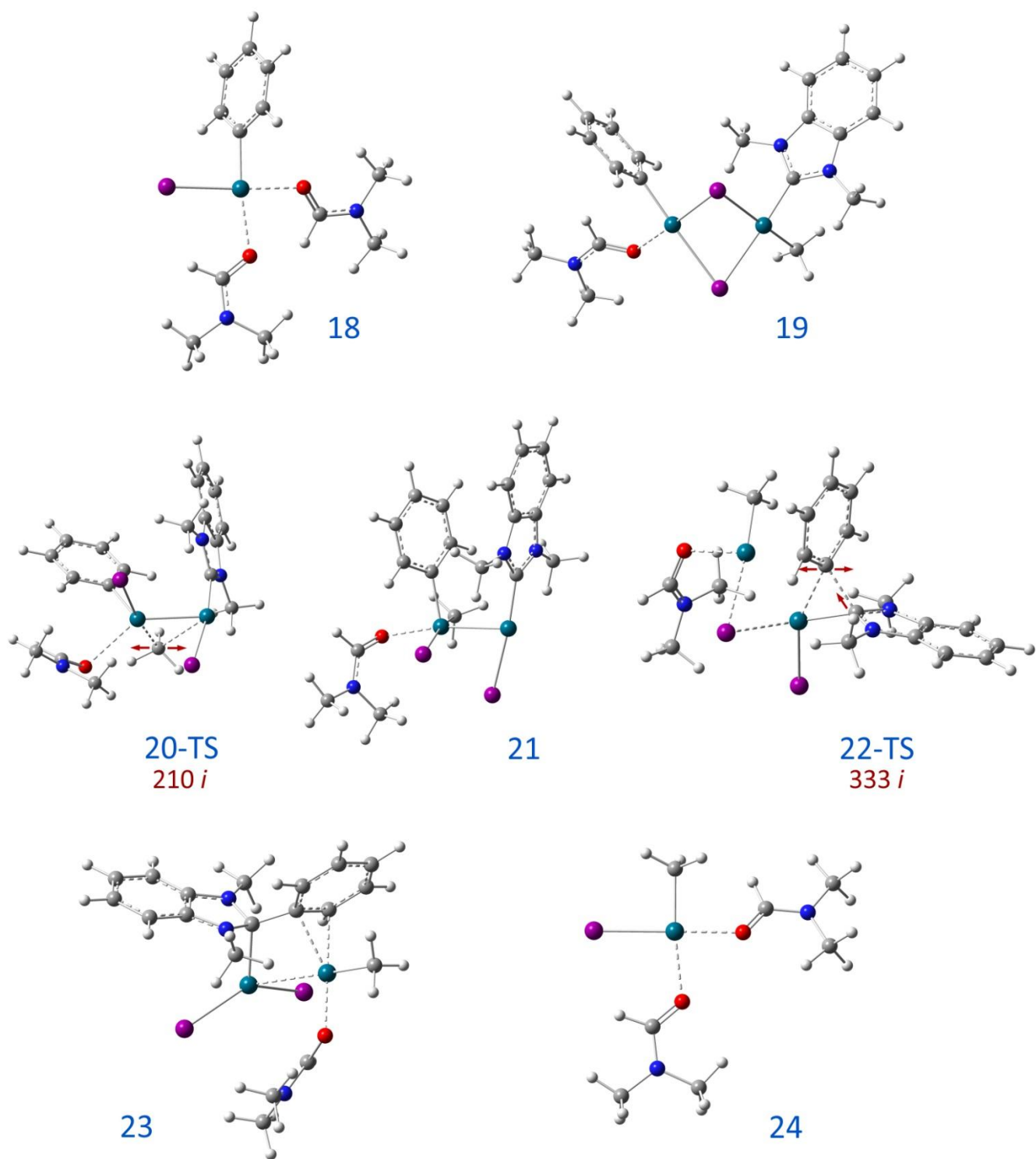


Figure S30. Optimized molecular structures for Figure S28. The imaginary frequencies and atomic displacements corresponding to imaginary vibration are represented for each transition state; PBE1PBE/6-311G(d)&def2TZVP D3BJ.

4. Ph-NHC coupling involving Pd(IV) complex formed by oxidative addition of Me-NHC to Pd(II) complex

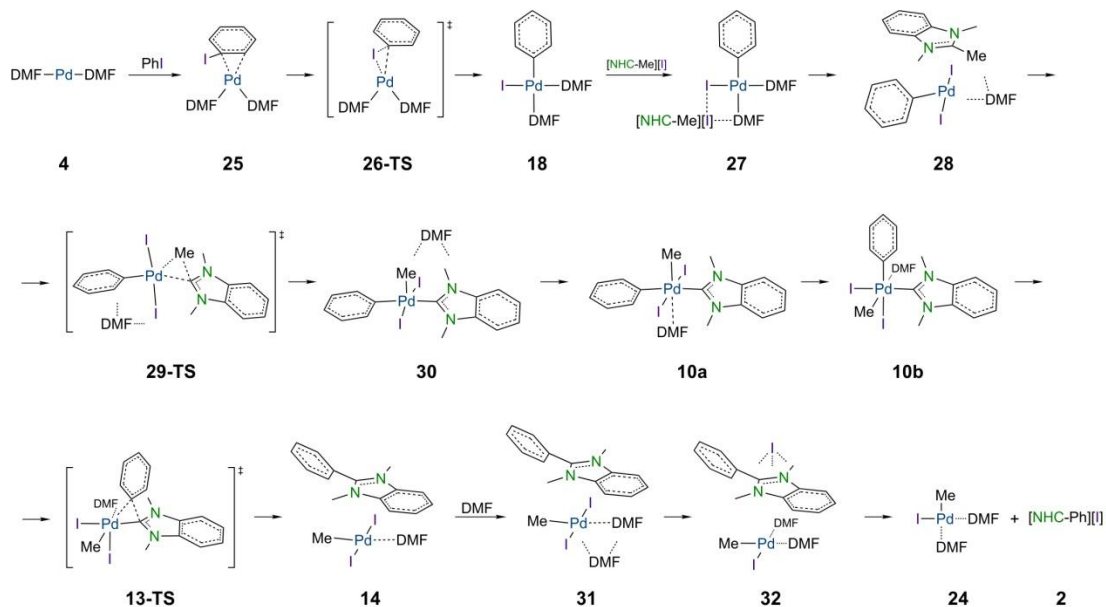


Figure S31. Reaction of Me-NHC addition/Ph-NHC coupling flowing through Pd(IV) complex. See Figure S35 for conformational analysis of complex **10**.

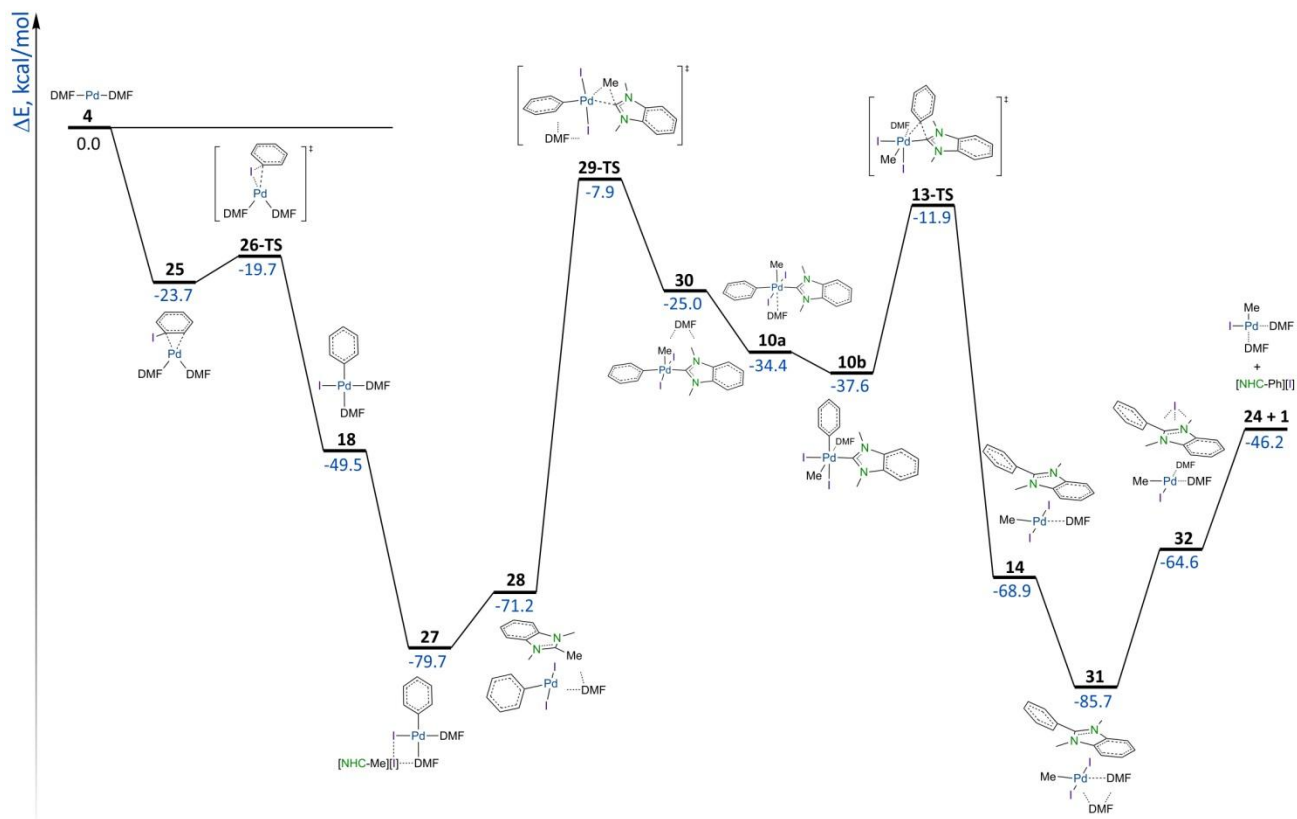


Figure S32. Potential energy surface of Me-NHC addition/Ph-NHC coupling reactions flowing through the Pd(IV) complex, PBE1PBE/6-311G(d)&def2TZVP D3BJ.

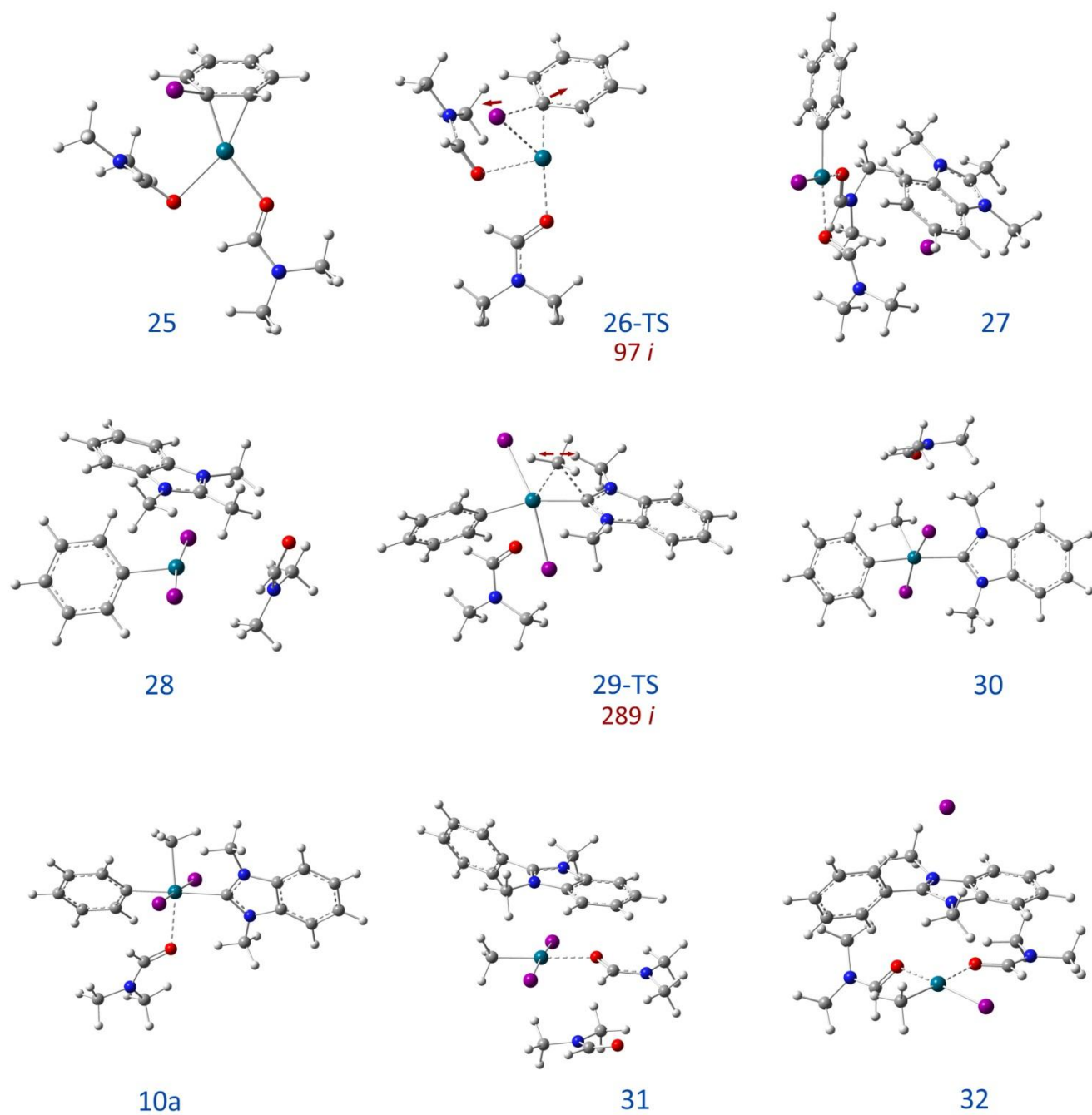


Figure S33. Optimized molecular structures for Figure S31. The imaginary frequencies and atomic displacements corresponding to imaginary vibration are represented for each transition state; PBE1PBE/6-311G(d)&def2TZVP D3BJ.

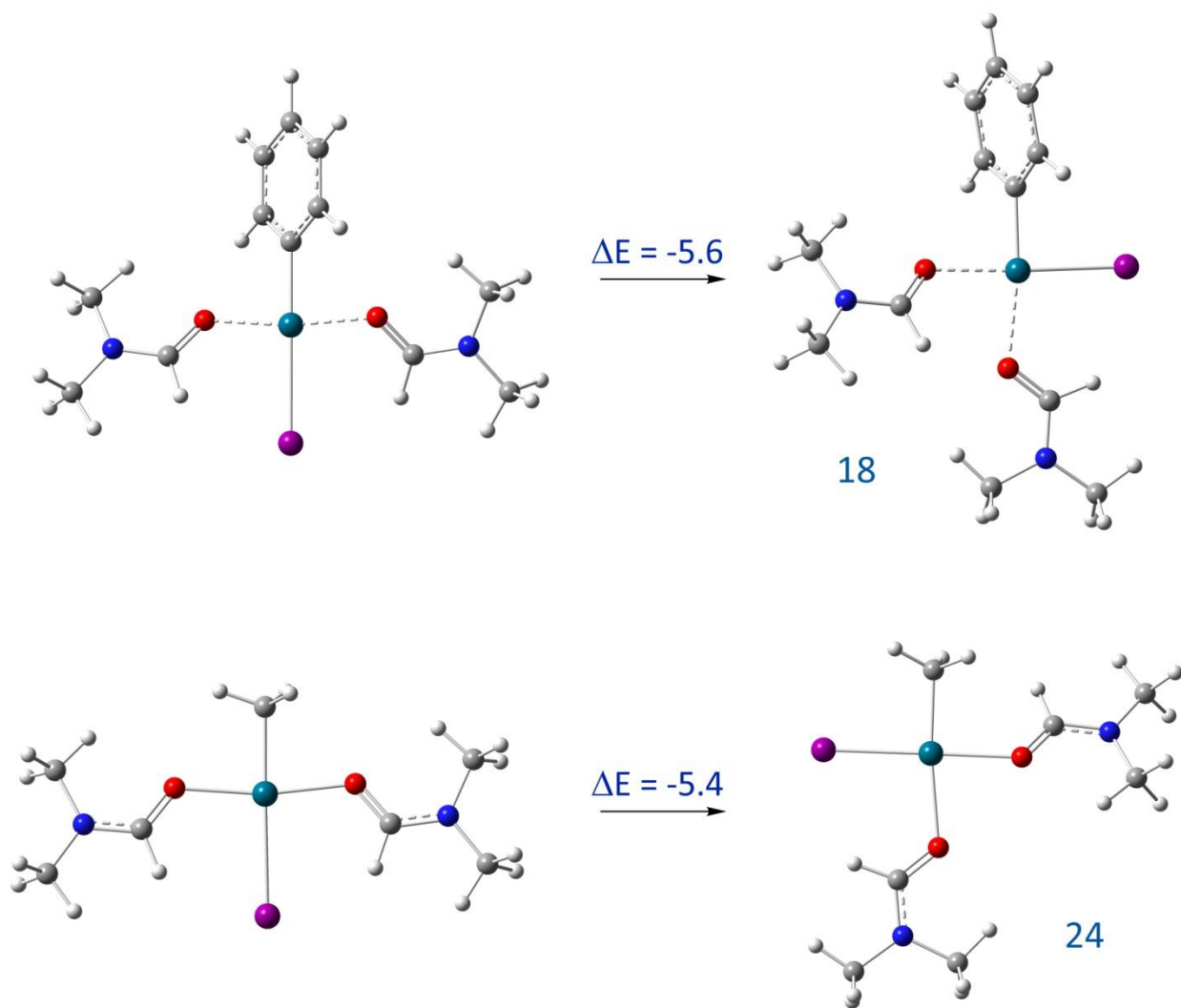


Figure S34. Molecular structures of isomers of complex **18** and **24** their relative energies (kcal/mol), PBE1PBE/6-311G(d)&def2TZVP D3BJ.

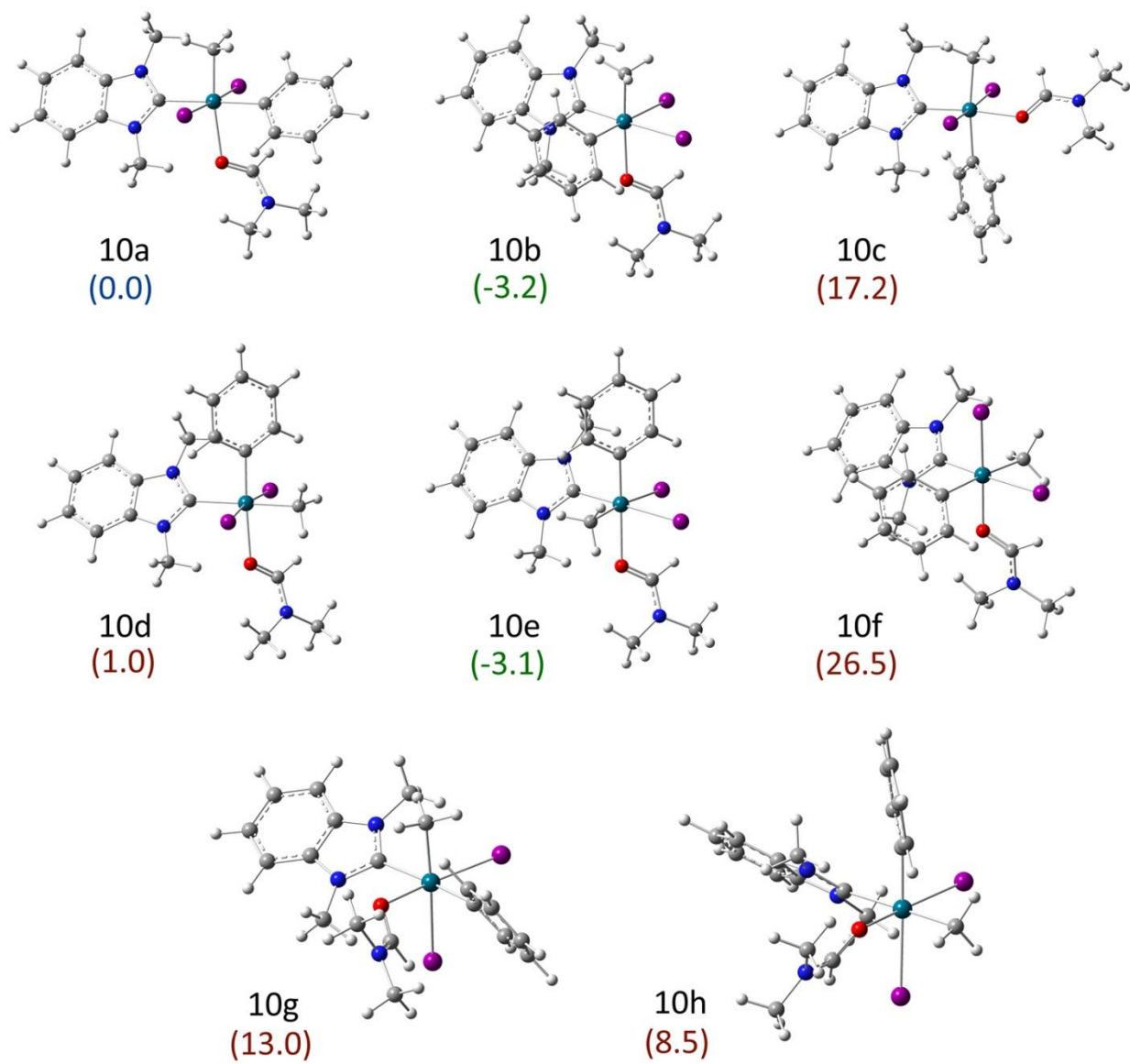


Figure S35. Molecular structures of isomers of complex **10** and their relative energies (kcal/mol), PBE1PBE/6-311G(d)&def2TZVP D3BJ.

5. Reductive elimination of MeI

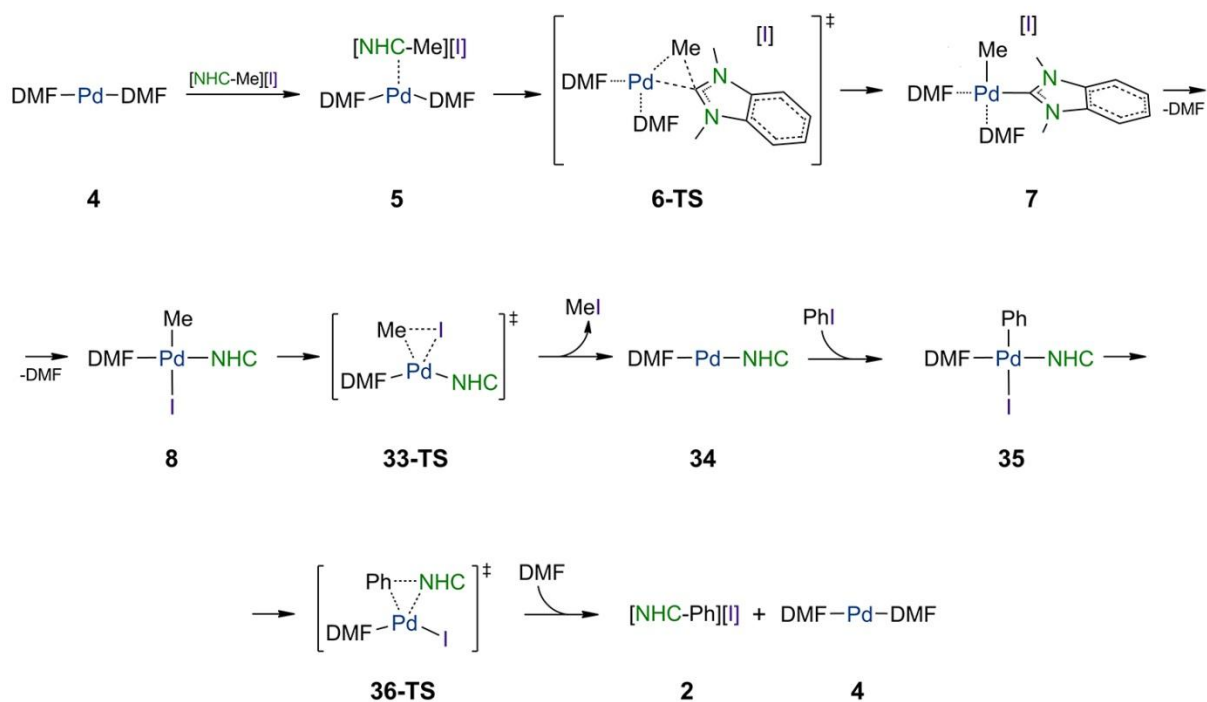


Figure S36. Reaction of reductive elimination of MeI.

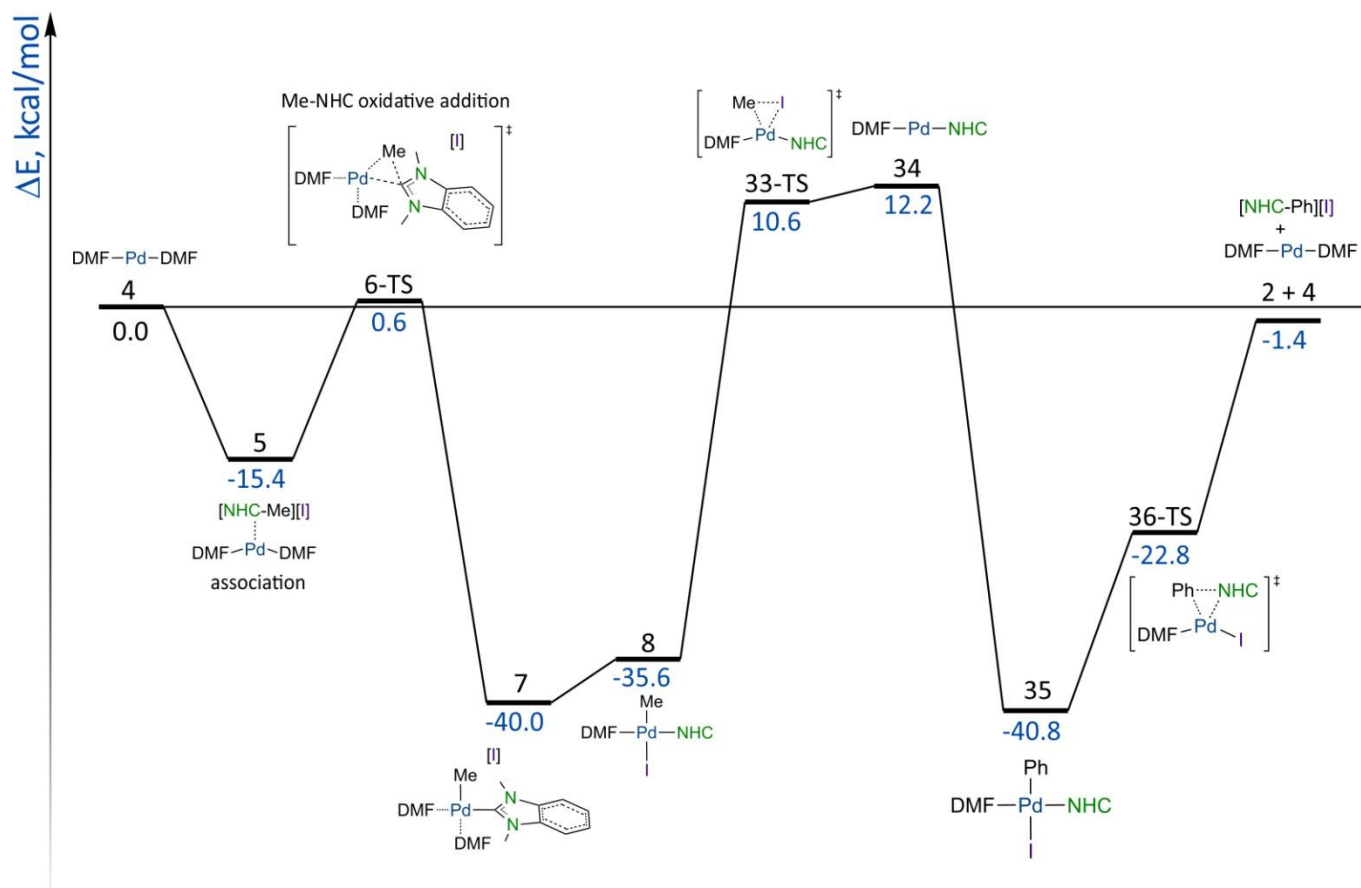


Figure S37. Profile of total energy changes during MeI elimination reaction.

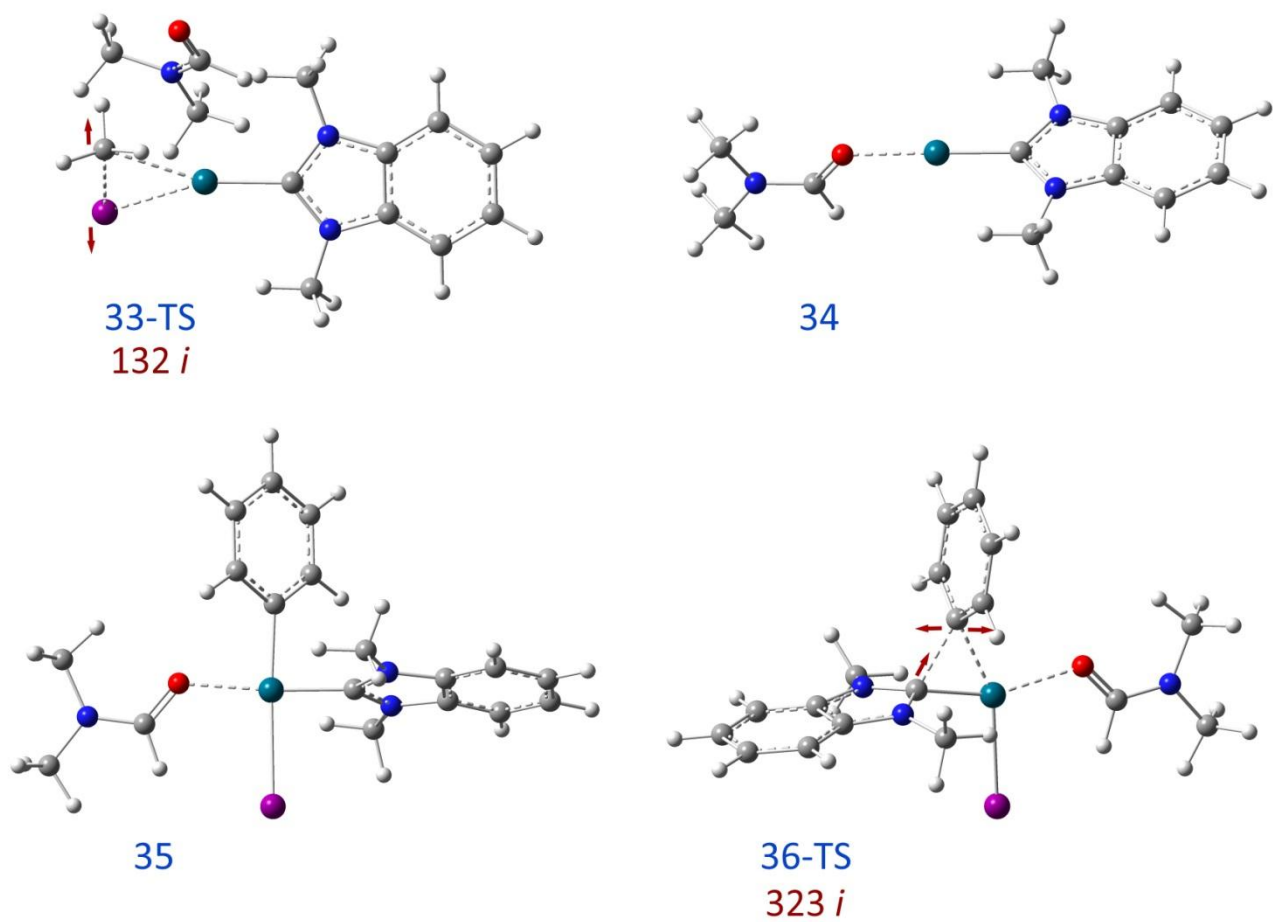


Figure S38. Optimized molecular structures for Figure S36. The imaginary frequencies and atomic displacements corresponding to imaginary vibration are represented for each transition state; PBE1PBE/6-311G(d)&def2TZVP D3BJ.

6. Proposed structure of $[(C_9H_{10}N_2)(C_{10}H_{13}N_2)I_2Pd(CH_3CN)]^+$

Experimental ESI-MS study detected Pd-containing positively charged ion with m/z 707.93 and the following formula can be proposed: $[(BIME)(Me-BIME)I_2Pd(CH_3CN)]^+$ (see Figure 2 for the structure of BIME ligand).

According to DFT calculations, the complex may adopt square configuration. In the calculated structural arrangement BIME ligand is bound to the metal and $[Me-BIME]^+$ fragment tends to connect predominantly via electrostatic interactions to one of the iodide ligands. Considerable binding energy of 21.2 kcal/mol was calculated for the $[Me-BIME]^+$ fragment (Figure S39). Calculated structure is in good agreement with observed dissociation pathways in CID MS² experiment (Figure S23).

Alternative arrangement of the $[Me-BIME]^+$ fragment may involve binding of Me- and BIME as ligands to the metal center and formation of $[(BIME)_2(Me)I_2Pd(CH_3CN)]^+$ octahedral complex. However, it is less likely due to substantial energy of such transition of 65.0 kcal/mol (Figure S39).

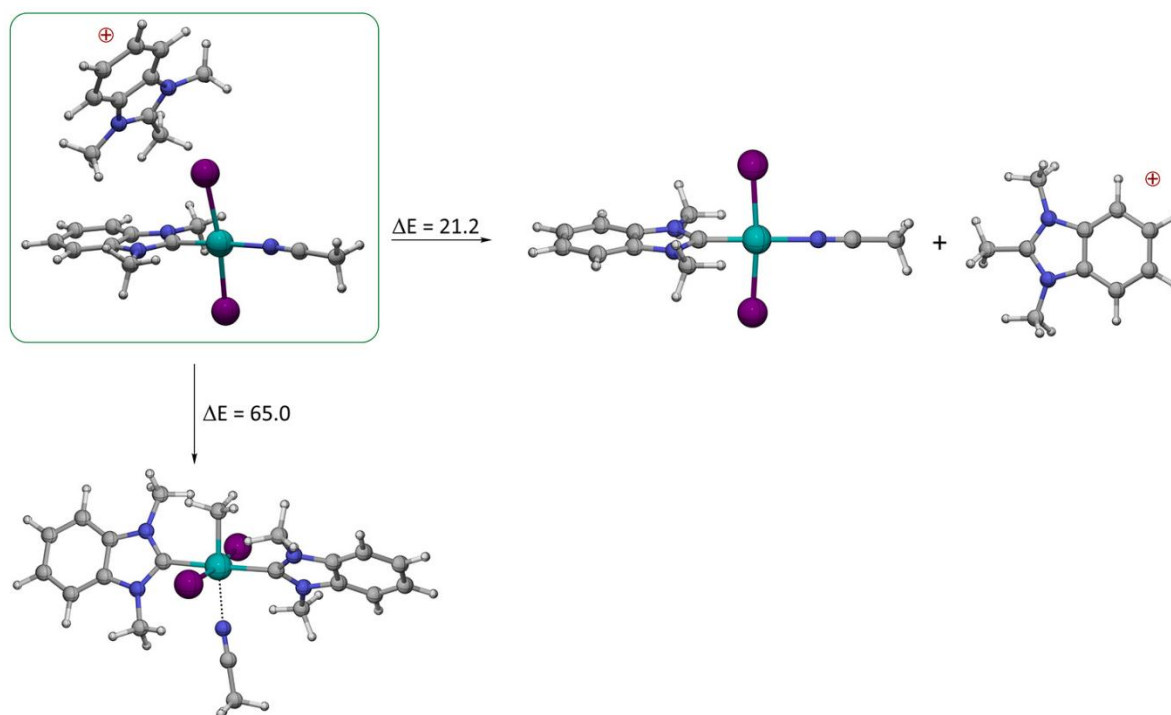


Figure S39. Molecular structures of possible isomers for the m/z 707.93 ion calculated at PBE1PBE/6-311G(d)&def2TZVP D3BJ level. Dissociated fragments and octahedral $[(BIME)_2(Me)I_2Pd(CH_3CN)]^+$ complex are higher in energy by 21.2 and 65.0 kcal/mol, respectively.